BOSTON UNIVERSITY

GRADUATE SCHOOL OF ARTS AND SCIENCES

Dissertation

MEASUREMENT OF THE ANOMALOUS MAGNETIC MOMENT OF THE POSITIVE MUON TO .SOMETHING PARTS PER BILLION

by

NICHOLAS BRENNAN KINNAIRD

B.S., University of Texas at Austin, 2013
B.S., University of Texas at Austin, 2013
M.A., Boston University, 2016

Submitted in partial fulfillment of the

requirements for the degree of

Doctor of Philosophy

2019

Approved by

First Reader

B. L. Roberts, PhD
Professor of Physics

Second Reader

R. M. Carey, PhD
Professor of Physics

Third Reader

J. P. Miller, PhD
Professor of Physics

Dedication

I dedicate this thesis to

Acknowledgments

Here go all your acknowledgments. You know, your advisor, funding agency, lab mates, etc., and of course your family.

As for me, I would like to thank Jonathan Polimeni for cleaning up old LaTeX style files and templates so that Engineering students would not have to suffer typesetting dissertations in MS Word. Also, I would like to thank IDS/ISS group (ECE) and CV/CNS lab graduates for their contributions and tweaks to this scheme over the years (after many frustrations when preparing their final document for BU library). In particular, I would like to thank Limor Martin who has helped with the transition to PDF-only dissertation format (no more printing hardcopies – hooray !!!)

The stylistic and aesthetic conventions implemented in this LaTeX thesis/dissertation format would not have been possible without the help from Brendan McDermot of Mugar library and Martha Wellman of CAS.

Finally, credit is due to Stephen Gildea for the MIT style file off which this current version is based, and Paolo Gaudiano for porting the MIT style to one compatible with BU requirements.

Janusz Konrad

Professor

ECE Department

MEASUREMENT OF THE ANOMALOUS MAGNETIC MOMENT OF THE POSITIVE MUON TO .SOMETHING PARTS PER BILLION

(Order No.)

NICHOLAS BRENNAN KINNAIRD

Boston University, Graduate School of Arts and Sciences, 2019

Major Professor: B. L. Roberts, Professor of Physics

ABSTRACT

This abstract was copied from my departmental seminar, and it needs to be updated for my thesis: One of the few indications for new physics is the discrepancy between the theoretical and experimental values for the anomalous magnetic moment of the muon. There is a 3 to 4 sigma discrepancy between theory and the last experimental measurement held at Brookhaven National Laboratory in 2001, which measured the muon g-2 to 540 parts per billion. This discrepancy has been consistent for many years now with ever improving theoretical calculations and other experimental measurements. In order to resolve or confirm this difference, a new experiment is underway at Fermilab to measure the muon g-2 to 4 times higher precision at 140 ppb. Muon g-2 at Fermilab gathered its first production data in 2018, and is currently taking data now. I will describe the principles of the experiment and detail two specific parts of the analysis that I have been involved in. These include track fitting and precession frequency analysis of the Run 1 data.

Contents

List of Tables

List of Figures

List of Abbreviations

BNL	....	Brookhaven National Laboratory
BSM	....	beyond the standard model
CBO	....	coherent betatron oscillation
E821	....	Brookhaven Muon $g-2$ Experiment
E989	....	Fermilab Muon $g-2$ Experiment
EW	....	electroweak
FID	....	free-induction decay
FNAL	....	Fermi National Accelerator Laboratory
Geane	....	Geometry and Error Propagation
Geant4	....	Geometry and Tracking 4
IBMS	....	inflector beam monitoring system
NMR	....	nuclear magnetic resonance
PMT	....	photo-multiplier tube
ppb	....	parts per billion
ppm	....	parts per million
ppt	....	parts per trillion
QCD	....	quantum chromodynamics
QED	....	quantum electrodynamics
SiPM	....	silicon photo-multiplier
SM	....	Standard Model
WFD	....	waveform digitizer

Chapter 1

Introduction

The prevailing theory for particle physics, the Standard Model (SM), has had tremendous success in describing our universe. It has been used to predict and explain a wide variety of phenomena, particles, properties, and interactions to great precision. However, in spite of its success in explaining nearly all experimental results, there remain unanswered questions about our universe. Some of these include the matter-antimatter asymmetry, the source of mass for the neutrinos, the existence of dark matter, and an inability to fully incorporate our best theory of gravitation. Many particle physics experiments around the world are being devised and conducted in order to shed light on these questions and improve our understanding of reality. One such particular experiment is the Fermilab Muon $g-2$ Experiment (E989) underway at the Fermi National Accelerator Laboratory (FNAL) located in Batavia, Illinois.

I have been a part of the E989 experiment since I began my graduate degree six years ago. Three years ago I moved from Boston to Batavia to get more involved by being where the action is. This dissertation will describe the E989 experiment and the work which I have done for it along the way in detail. Chapter 1 will provide experimental and theoretical background to the experiment, as well its motivation. Chapter 2 will describe the experimental principle. Chapter 3 will describe the magnetic field portion of the experiment, and magnetic field simulations I conducted. Chapter 4 will describe the straw tracking detectors and their measurements, including the track fitting I wrote. Chapter 5 will describe the frequency measurement portion of the experiment, and detail my analysis results from data taken in the first half of 2018. Finally, Chapter 6 will concluded the thesis and the results contained within.

1.1 Magnetic Moments of Particles

In order to understand the purpose of the Fermilab Muon $g-2$ Experiment, first we need to understand what the g in $g-2$ is. This is what the experiment is measuring. All particles have intrinsic properties. One of those properties is the magnetic dipole moment.[1] This property of a particle is related to its spin through the equation

$$\vec{\mu} = g\frac{q}{2m}\vec{s}, \tag{1.1}$$

where $\vec{\mu}$ is the magnetic dipole moment of a particle, $\vec{s}$ is its spin vector, m is its mass, $q = \pm e$ where e is the elementary charge, and g is the so called "g-factor". g is some measurable and predictable constant, which as shown in Equation 1.1 relates the magnetic moment of a particle to its spin angular momentum. Since the torque on a particle in a magnetic field is

$$\vec{N} = \vec{\mu} \times \vec{B}, \tag{1.2}$$

the rate at which a particles spin precesses in a magnetic field will depend on g. This happens to be one of the key physics principles in the E989 experiment as will be discussed later.

In a Dirac theory, g is equal to 2 for spin-1/2 particles with no internal structure [1]. See Appendix A for a nice derivation of this result. It turns out however, that g is not quite equal to 2 even for these types of particles. Motivated by early experimental discrepancies such as the measurements of the hyperfine structure in hydrogen [2],

[1] *Magnetic dipole moment* and *magnetic moment* are equivalent when talking about particles.

in 1948 Schwinger calculated the first ”radiative correction” to the electron magnetic moment [3]. In a quantum field theory, interactions of the particle with virtual particles in loops will contribute to the value of g. In this context it is nicer to recast the magnetic dipole moment formula as

$$\begin{aligned} \vec{\mu} &= 2(1+a)\frac{q}{2m}\vec{s}, \\ a &= \frac{g-2}{2}, \end{aligned} \tag{1.3}$$

where a is called the ”anomalous” part of the magnetic moment, and contains all higher order corrections. The first correction calculated to a by Schwinger was $a = \alpha/2\pi \approx 0.00116$, where α is the fine structure constant. By measuring a, the SM theory can be tested and extensions to it constrained. The measurement of the anomalous piece of the muon is indeed where the Fermilab Muon $g-2$ Experiment gets its name.

1.2 Standard Model Contributions to a_μ

(Double check all numbers and make sure the correlations in the final result are considered appropriately. Make sure latest theoretical results are included.)

Before experimental results have any real meaning, they need a theory with which to compare. The latest theoretical predictions for the muon magnetic moment will be presented here. The contributions to a_μ can be summed from separate pieces relating to different parts of the SM. These include the quantum-electrodynamics (QED) corrections purely from other leptons and photons, the electroweak (EW) corrections from interactions with the weak force bosons $W^\pm$ and Z^0, and the hadronic corrections from interactions with hadrons:

$$a_\mu^{\mathrm{SM}} = a_\mu^{\mathrm{QED}} + a_\mu^{\mathrm{EW}} + a_\mu^{\mathrm{Had}} \tag{1.4}$$

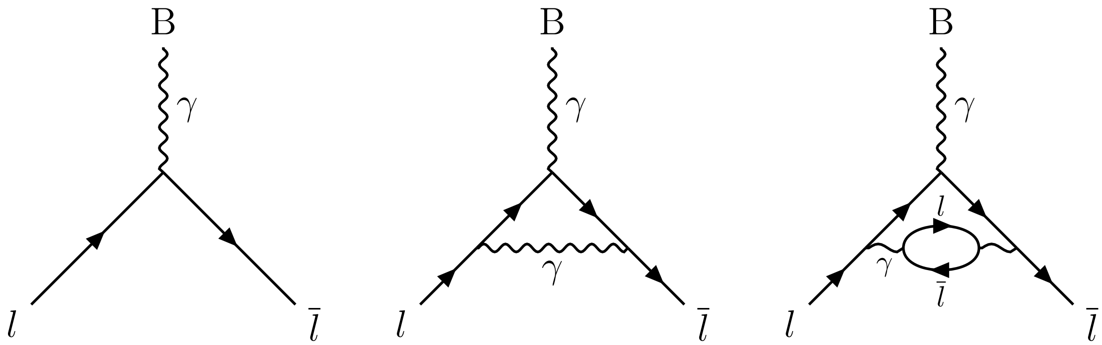

(a) Dirac result, $g = 2$.

(b) The first loop diagram, calculated by Schwinger.

(c) A two loop diagram.

Figure 1·1: The first of many QED diagrams contributing to a. B is an external magnetic field. Feynman diagrams made with [6, 7].

1.2.1 QED

The QED contributions to a_μ stem solely from loops with virtual leptons and photons. They are very well understood and have been calculated to very high order, having been calculated up to five loop level from over 12,000 Feynman diagrams [4, 5]. This has been done either analytically or numerically. The first couple of diagrams including the Dirac $g = 2$ and Schwinger diagrams are shown in Figure 1·1. The value is

$$\begin{aligned} a_\mu^{\text{QED}} &= \sum_{n=1}^{\infty} C_n \left(\frac{\alpha}{\pi}\right)^n, \\ &= (11658471.8971 \pm 0.0007) \times 10^{-10}, \end{aligned} \tag{1.5}$$

where in the first line a_μ^{QED} is expressed as a perturbative expansion of the fine structure constant. $C_1 = 1/2$ is the Schwinger result mentioned previously stemming from the diagram shown in Figure 1·1b. Over 99% of the value of a_μ comes from the QED sector, but the error is much smaller than the other contributions, as well as the experimental uncertainty.

1.2.2 Electroweak

The electroweak contributions to a_μ are known to two loop level, with some three loop parts estimated. The contributions stem from couplings with the heavy weak gauge bosons. The different one loop diagrams and an example two loop diagram are shown in Figure 1·2. Per usual Feynman rules, the propagators will contain the masses of the interacting bosons, while the kinematics will contain the masses of the leptons. For calculations of a muon in the case of Figure 1·2a, these result in a factor $\sim (m_\mu/m_{Z^0})^2$. Because the mass of the gauge bosons are so much more than the muon, these processes are necessarily suppressed and the electroweak contributions to a_μ are small. For this reason knowing these contributions only up to two loop level is sufficient. The value of the electroweak contributions is

$$a_\mu^{\mathrm{EW}} = (15.12 \pm 0.01) \times 10^{-10}, \tag{1.6}$$

with improvements having been made recently [8, 9]. Again the error on these contributions is small compared to the hadronic contributions discussed next, as well as the experimental uncertainty.

1.2.3 Hadronic

The hadronic contributions to a_μ stem from interactions with hadrons. Because they cannot be calculated perturbatively at low energies due to the QCD nature of these particles, these calculations comprise the dominant uncertainty in the SM calculation. This makes their error estimation extra important when comparing to experiment. Most active work on the theoretical side of things is in this sector. These contributions can be separated into two parts

$$a_\mu^{\mathrm{Had}} = a_\mu^{\mathrm{HVP}} + a_\mu^{\mathrm{HLbL}}. \tag{1.7}$$

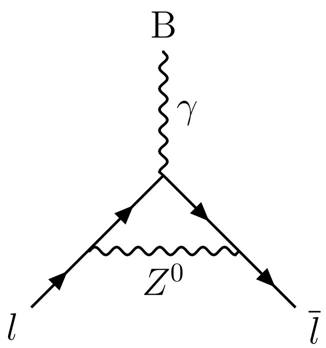

(a) Exchange of a virtual Z^0 boson.

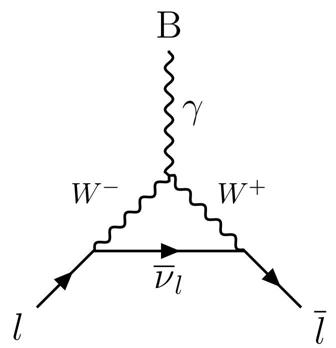

(b) Electroweak loop with W bosons.

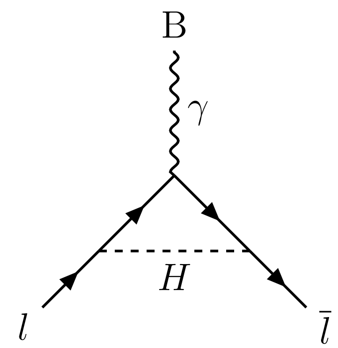

(c) Exchange of a Higgs boson.

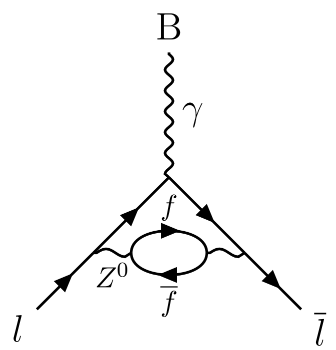

(d) Second order electroweak diagram.

Figure 1·2: First order (and one second) weak diagrams contributing to a. B is an external magnetic field. Feynman diagrams made with [6, 7].

Hadronic Vacuum Polarization

The first of these hadronic contribution parts is the hadronic vacuum polarization part (HVP), the first order diagram of which is shown in Figure 1·3a. There are two main prescriptions for calculating these contributions. The first is to use a dispersive approach to introduce a virtual hadron blob into the integral calculation for the photon propagator [10], and then utilize the optical theorem to relate the imaginary part of that propagator to the total cross-section of electron-positron annihilation to hadrons. While this could be solved perturbatively for a lepton blob in place of the hadron blob, this is instead a data driven approach when considering non-perturbative QCD. The details of dispersion theory will not be described here. The leading order contribution can be written as

$$a_\mu^{\text{HVP;LO}} = \left(\frac{\alpha m_\mu}{3\pi}\right)^2 \int_{m_\pi^2}^{\infty} \frac{ds}{s^2} K(s) R(s) \tag{1.8}$$

where $K(s)$ is some kinematic factor, and $R(s)$ is a ratio of cross-sections

$$R(s) = \frac{\sigma(e^+e^- \to \text{hadrons})}{\sigma(e^+e^- \to \mu^+\mu^-)}. \tag{1.9}$$

The cross-section data for this relation has been measured in parts by various experiments, including KLOE, CLEO, BaBar, and BESIII [11, 12, 13, 14]. The analysis by Keshavarzi et al. [15] gives results as

$$\begin{aligned} a_\mu^{\text{HVP;LO}} &= (693.26 \pm 2.46) \times 10^{-10}, \\ a_\mu^{\text{HVP;NLO}} &= (-9.82 \pm 0.04) \times 10^{-10}, \end{aligned} \tag{1.10}$$

where $a_\mu^{\text{HVP;NLO}}$ is the next to leading order calculation. This calculation is consistent with Davier et al. [16]. In this way, the SM theory has some dependence on experimental results. This is acceptable as the experimental measurements are

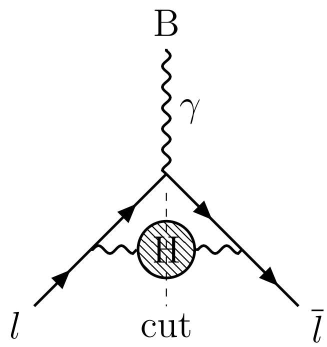

(a) The first order HVP diagram. The blob H in the middle indicates any combination of hadrons which satisfy the Feynman rules.

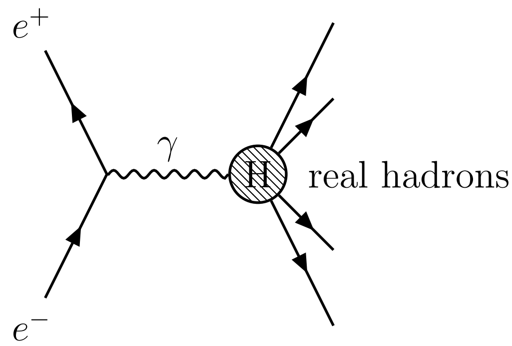

(b) The Feynman diagram for electron positron annihilation to hadrons.

Figure 1·3: The first order HVP diagram on the left, which can be related to the diagram on the right by making a 'cut' across the virtual hadrons blob. B is an external magnetic field. Feynman diagrams made with [6, 7].

straightforward observables.

The second prescription to estimating the HVP contributions is a first principles approach, using lattice QCD and QED. It is a gauge theory defined on a matrix of points in time and space. Once the matrix is taken infinitely large with the spacing between the points infinitely small, the behavior from a continuous theory is recovered. The results for the leading order estimates of $a_\mu^{\mathrm{HVP;LO}}$ are consistent with those provided above, though the error is larger. If the calculation is supplemented with the cross-section data described above, then this method provides the most precise determination of $a_\mu^{\mathrm{HVP;LO}}$ [17].

Hadronic Light-by-Light

The second of these hadronic contribution parts is a higher order four photon interaction, termed hadronic light-by-light. Diagrams are are shown in Figure 1·4. Again perturbation theory is unable to assist in the calculation of these contributions. For a

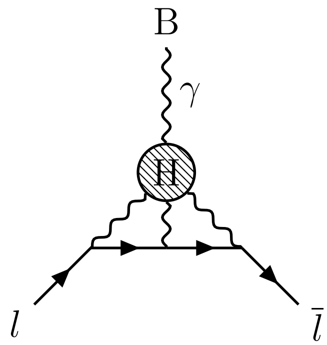

(a) The first HLbL diagram, where three photons are exchanged with some virtual hadrons blob.

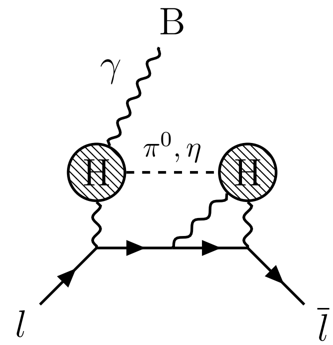

(b) A second HLbL diagram, where three photons are exchanged with two virtual hadrons blobs, that are connected with some virtual chargeless propagator.

Figure 1·4: HLbL diagrams contributing to a_μ. B is an external magnetic field. Feynman diagrams made with [6, 7].

long time the calculation of these diagrams was model dependent, and has therefore been the most contentious part of the SM calculation. In more recent years, there have been efforts to produce results using dispersive and lattice approaches [18]. In accordance with all of this, the error on this contribution is large, comparable to that of the $a_\mu^{\mathrm{HVP;LO}}$ term, even though the size of this contribution is small. The value of the HLbL contributions to a_μ quoted by Keshavarzi et al. and given by Nyffeler [15, 19] comes from model estimates and is

$$a_\mu^{\mathrm{HLbL}} = (9.8 \pm 2.6) \times 10^{-10}. \tag{1.11}$$

1.2.4 Combined Standard Model Value

The sum of the a_μ contributions listed here is

$$\begin{aligned} a_\mu^{\mathrm{SM}} &= a_\mu^{\mathrm{QED}} + a_\mu^{\mathrm{EW}} + a_\mu^{\mathrm{Had}}, \\ &= (11659180.26 \pm 3.58) \times 10^{-10}. \end{aligned} \tag{1.12}$$

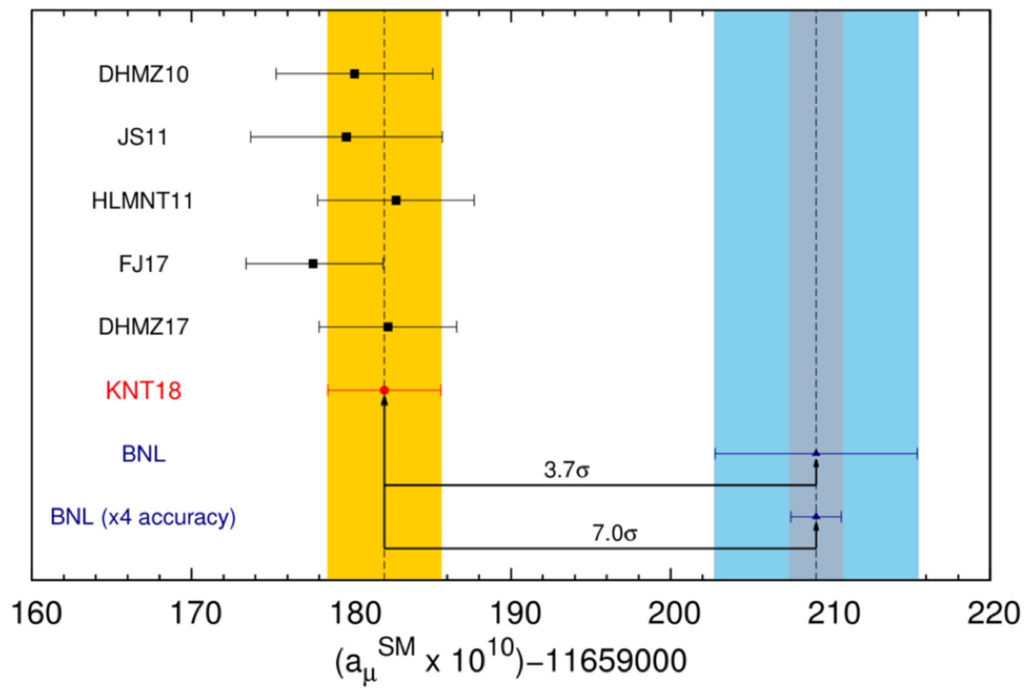

Figure 1·5: Various theoretical values for a_μ on the left, as compared to the most recent and extrapolated experimental result on the right. Plot courtesy of Alex Keshavarzi [15].

The relative uncertainty of this result is 307 ppb. Other analyses with different values for the various contributions typically agree well, as shown on the left side of Figure 1·5. Depending on what calculations are used, the discrepancy between theory and experiment ranges from 3-4 σ. The latest experimental result is described in the following section.

1.3 Experimental Value of a_μ and Discrepancy with a_μ^{SM}

The theoretical contributions to a_μ listed in the previous sections have improved over time as methods have matured and more experimental data gathered. Similarly, work on the direct experimental measurement of a_μ has been going on for decades, with more precise results being determined over time [20]. The most recent experiment to measure $g-2$ was the Brookhaven Muon $g-2$ Experiment (E821) held at Brookhaven National Laboratory (BNL) in 2001 [21]. That experiment measured a value for a_μ of

$$a_\mu^{\mathrm{Exp}} = (11659208.0 \pm 6.3) \times 10^{-10}, \tag{1.13}$$

which corresponds to a 540 ppb relative uncertainty. Note that the uncertainty of the experimental measurement is comparable to that of the theory, necessitating precise understanding of all the different theoretical parts. The difference between the experimental and theoretical values here is

$$a_\mu^{\mathrm{Exp}} - a_\mu^{\mathrm{SM}} = (27.74 \pm 7.25) \times 10^{-10}, \tag{1.14}$$

corresponding to a discrepancy of 3.83σ from 0.

-double check the numbers here later on down the line, values like a_μ experimental may even have changed if other constants have changed

1.4 Beyond the Standard Model and the Purpose of E989

While the discrepancy between experiment and theory might be attributed to miscalculations in the theory or systematic errors in the E821 experiment, no such errors have been found despite serious attempts to resolve the two. Indeed the discrepancy has only grown over time as the theoretical calculations have matured. The most intriguing and exciting source of the discrepancy would be physics beyond the standard model (BSM). Since the value of a_μ receives contributions from all particles that couple to the muon through virtual loops, unknown particles might be the source of this discrepancy. Specifically, since the contribution to the magnetic moment from

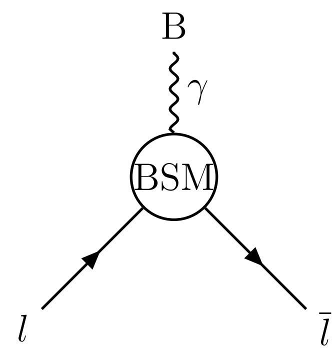

Figure 1·6: An example Feynman diagram, where the leptons couple to an external magnetic field B through some BSM physics. Feynman diagrams made with [6, 7].

heavy virtual particles goes as

$$a \sim \frac{m^2}{\Lambda^2}, \tag{1.15}$$

where Λ is the mass scale of the new particle and m the mass of the lepton in question, the sensitivity of the muon as compared to the electron to large mass scales is $m_\mu^2/m_e^2 \approx 43000$ greater. It is possible from this reason that even though the magnetic moment of the electron has been measured extraordinarily precisely, to .26 parts per trillion (ppt) [22, 23], it has provided no indication of anything new, whereas the magnetic moment of the muon might provide definitive evidence of new physics.

A basic example diagram of new physics is shown in Figure 1·6. Because the discrepancy from the previous experiment was not at the 5σ level necessary to classify it as a discovery, the E989 experiment was undertaken. Indeed with the lack of new physics results coming out of the LHC and other experiments, E989 is especially positioned to uncover something new at a time where there are so few hints of new physics. Because of this, the interest in the E821 experiment and underway E989 experiment has only grown over time. The number of citations for the E821 results has been consistently high over the years and is shown in Figure 1·7.

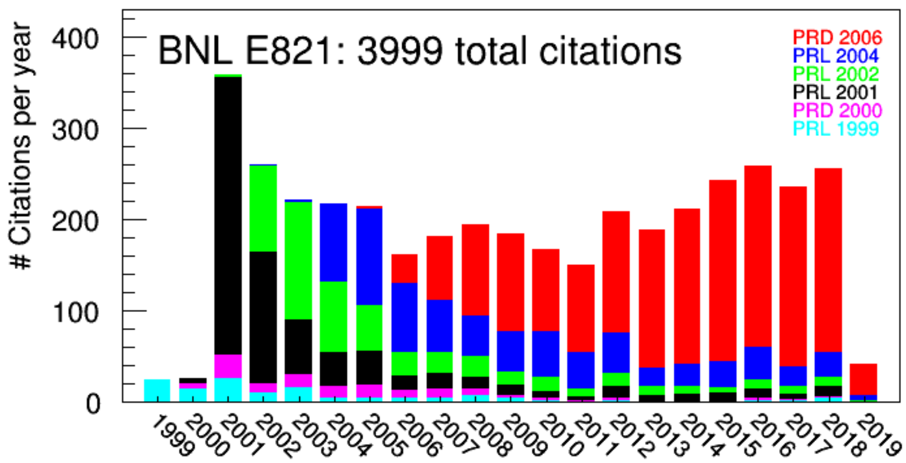

Figure 1·7: The number of citations for the BNL experiment publications as a function of year. Plot courtesy of Lee Roberts.

The E989 experiment has the goal of measuring a_μ to 140 ppb over the course of several years. This would be a factor of 4 improvement over the E821 result stemming from a 20 times increase in statistics, which was the limiter in the previous experiment. Assuming the same value for a_μ is measured, this would push the discrepancy over the 5σ mark to approximately 7σ, as shown in Figure 1·5. The data comprising Run 1, gathered in the spring and summer of 2018, is the subject of this thesis, and corresponds to an experimental uncertainty comparable to the E821 result. When it's all said and done, the hope is that we measure something new and exciting, pushing the discrepancy out beyond the 5σ level. Even if we do not however, it is valuable in itself to resolve this theoretical and experimental conflict.

Chapter 2

Principle Techniques of E989

As referenced in Equation 1.2, a particle in a magnetic field will experience a torque which attempts to line up the magnetic dipole moment of the particle with the external field. Because of this, in a dipole field a particles spin will turn at the Larmor precession frequency [24]

$$\vec{\omega}_s = -g\frac{q}{2m}\vec{B} - (1-\gamma)\frac{q}{\gamma m}\vec{B}, \tag{2.1}$$

where as before m is the particles mass, $q = \pm e$ where e is the elementary charge, g is the g-factor, γ is the Lorentz relativistic factor, and B is an external magnetic field. The second term is a relativistic correction to the precession frequency called Thomas precession [24]. Similarly, a particle with some momentum will orbit at the cyclotron frequency

$$\vec{\omega}_c = -\frac{q}{\gamma m}\vec{B}. \tag{2.2}$$

By taking the difference between these two frequencies we arrive at the "spin difference frequency"

$$\vec{\omega}_a = \vec{\omega}_s - \vec{\omega}_c = -\frac{g-2}{2}\frac{q}{m}\vec{B} = -a\frac{q}{m}\vec{B}, \tag{2.3}$$

a frequency that is directly proportional to the anomalous magnetic moment a. Briefly note that if $g = 2$ as in a Dirac theory, then the particles spin would turn at the same rate as the momentum vector, and this spin difference frequency ω_a would be identically 0. If this spin difference frequency for a muon and the external magnetic dipole field can be measured, then the anomalous magnetic moment of the muon a_μ can be measured.

As will be detailed below in Section 2.2, the measurement of the magnetic field is related to the Larmor precession frequency of free protons in water

$$\omega_p = -g_p \frac{e}{2m_p} B, \tag{2.4}$$

where g_p and m_p are the g-factor and mass of the proton respectively. Replacing B and solving for a_μ, we arrive at

$$a_\mu = \frac{g_p}{2} \frac{\omega_a}{\omega_p} \frac{m_\mu}{m_p}. \tag{2.5}$$

Using the magnetic moment formulas for the proton, electron, and muon as shown in Equation 1.1, Equation 2.5 can be transformed to either of the following consistent equations:

$$\begin{aligned} a_\mu &= \frac{g_e}{2} \frac{\omega_a}{\omega_p} \frac{m_\mu}{m_e} \frac{\mu_p}{\mu_e} \\ a_\mu &= \frac{\omega_a/\omega_p}{\lambda - \omega_a/\omega_p} \end{aligned} \tag{2.6}$$

Here the p, e, and μ subscripts stand for the relevant quantities for the proton, electron, and muon respectively. In the second equation $\lambda = \mu_\mu/\mu_p$. As mentioned before the electron g-factor g_e has been measured to extremely high precision, 0.26 ppt [22, 23]. The muon-electron mass ratio m_μ/m_e and muon-proton magnetic moment ratio λ have been measured to 22 ppb [23, 25]. Finally the proton-electron magnetic moment ratio μ_p/μ_e has been measured to 3 ppb [23]. The errors on these terms are small compared to the target uncertainty for E989 of 140 ppb, the measurement of which now comes down to measuring the ratio ω_a/ω_p.

2.1 Measuring ω_a

How can ω_a for muons be measured? The answer lies with two key points in the dynamics of muon decay. Positive muons decay to a positron and two neutrinos, as shown in Figure 2·1a. The first point is that because of the parity violating nature of the weak interaction, the decay positron will be preferentially emitted right-handed, with its spin directed in the same direction as its momentum [26]. The second key point is that angular momentum must be conserved. Consider the most extreme examples of maximum and minimum energy positrons as shown in Figure 2·2. In the muon rest frame, decay positrons with maximum energy will be emitted opposite to the two neutrinos. Since neutrinos and anti-neutrinos must be left and right-handed respectively, thus having their spins anti-parallel and parallel to their momentum, by the law of conservation of angular momentum the positron must have its spin be parallel to the spin of the muon at the time of the decay. By the opposite argument, decay positrons emitted with minimum energy such that the neutrinos are ejected opposite to one another must have their spins be anti-parallel to that of the muon at the time of decay. These two points combined together means that higher energy decay positrons will preferentially be emitted in directions parallel to the muon spin at the time of decay, while lower energy decay positrons will preferentially be emitted in directions anti-parallel to the muon spin at the time of the decay.

This correlation between the emitted direction of the decay positron and the spin of the muon is the signature needed to measure ω_a. By placing an ensemble of polarized muons within a magnetic storage ring, those muons will orbit at the cyclotron frequency and their spins will precess at the Larmor frequency. As they go around the ring they will decay to positrons whose energy and decay directions contain information about the spin of the muon. The differential decay distribution

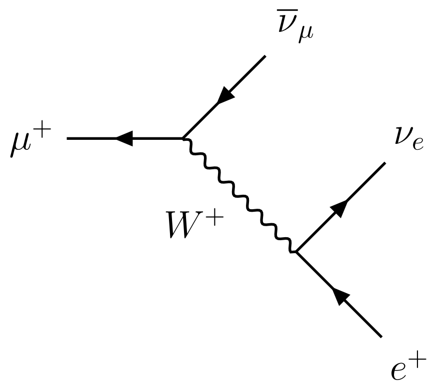

(a) μ^+ decay through a W^+ boson to a positron, muon anti-neutrino, and an electron neutrino. This is the dominant decay mode.

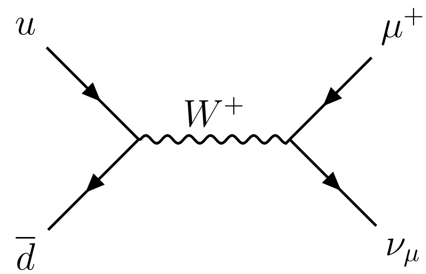

(b) π^+ decay through a W^+ boson to a μ^+.

Figure 2·1: Feynman diagrams for muon (left) and pion (right) decay.

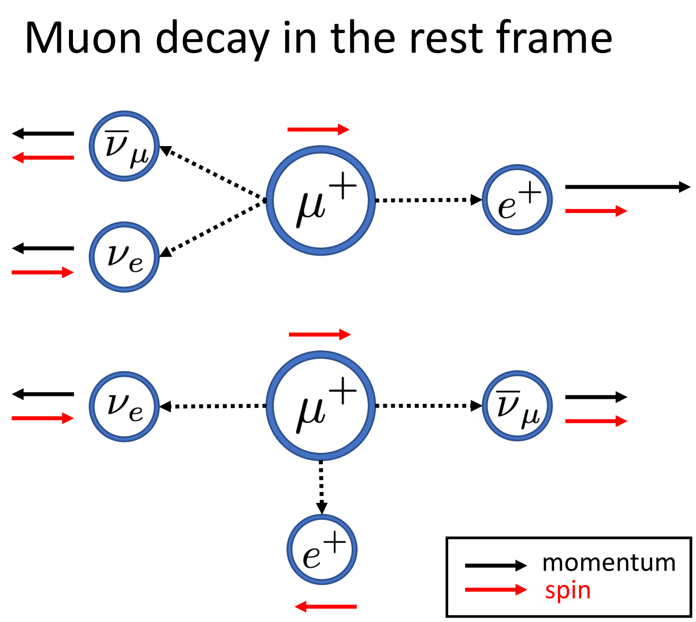

Figure 2·2: Muon decay pictures for maximum and minimum energy decay positrons. Due to the conservation of angular momentum and the single possible helicity states of the decay neutrinos, the spin of the decay positron is exactly parallel to the spin of the muon at the time of the decay for maximum energy decay positrons (top), or anti-parallel for minimum energy decay positrons (bottom).

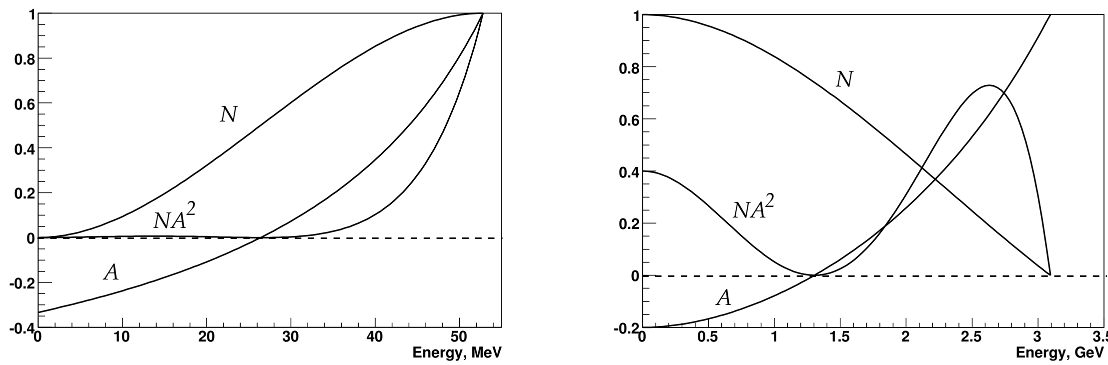

(a) Muon rest frame (b) Lab frame

Figure 2·3: Decay number distribution N and asymmetry A in the muon rest frame (left) and in the lab frame (right) as a function of positron energy with a maximum positron energy of 3.1 GeV.

in the muon rest frame is described by [26]

$$dP(y, \theta) \propto N(y)[1 \pm A(y)\cos(\theta)]dyd\Omega, \tag{2.7}$$

where $y = E/E_{max}$ is the energy fraction of the positron, θ is the angle between the spin of the muon and the momentum of the positron $\cos^{-1}(\hat{p} \cdot \hat{s})$, and the $\pm$ stands for the positive and negative muon respectively. $N(y)$ is the number distribution of decay positrons and $A(y)$ is the so called 'asymmetry' encoding the preferred positron decay direction. Here the energy of the positron is assumed to be much greater than its mass. The number distribution and asymmetry are given by [26]

$$N(y) = 2y^2(3 - 2y^2), \tag{2.8}$$

$$A(y) = \frac{2y - 1}{3 - 2y}, \tag{2.9}$$

and are shown in Figure 2·3a.

In the lab frame for high energy positrons, nearly all positrons will be emitted parallel to the muon momentum, which makes it challenging to select purely on the decay angle of the positron. That's not a problem though, as we already know that decay positrons with higher energies will be emitted in directions parallel to the muon spin at the time of decay. Essentially, the energy distribution of detected positrons for high energies is modulated by ω_a, or $\theta = \omega_a t + \phi$. The number of detected positrons at some time and energy in the lab frame for some initial number N_0 of muons can then be described by

$$N_d(t, E) = N_0(E) \cdot e^{-t/\gamma\tau_\mu} \cdot [1 + A(E)\cos(\omega_a t + \phi(E))], \tag{2.10}$$

where the d subscript stands for 'detected,' the muons are decaying at a lifetime of $\gamma\tau_\mu$, and all the relevant parameters are energy dependent. Here $N_0(E)$ and $A(E)$ have been transformed from Equations 2.8 and 2.9 to the lab frame,

$$N_0(E) \propto (y-1)(4y^2 - 5y - 5), \tag{2.11}$$

$$A(E) = \frac{-8y^2 + y + 1}{4y^2 - 5y - 5}, \tag{2.12}$$

where as a reminder $y = E/E_{max}$. Here the polarization of the muons is assumed to be unity. These are shown in Figure 2·3b. To increase the amount of statistics, all positrons above some energy threshold cut E_{th} can be taken as the observable,

$$N_d(t, E_{th}) = N_0(E_{th}) \cdot e^{-t/\gamma\tau_\mu} \cdot [1 + A(E_{th})\cos(\omega_a t + \phi(E_{th}))], \tag{2.13}$$

where the number and asymmetry of the detected positrons is now calculated by simply integrating Equations 2.11 and 2.12 from y_{th} to 1,

$$N_0(E_{th}) \propto (y_{th} - 1)^2(-y_{th}^2 + y_{th} + 3), \tag{2.14}$$

$$A(E_{th}) = \frac{y_{th}(2y_{th} + 1)}{-y_{th}^2 + y_{th} + 3}, \tag{2.15}$$

where $y_{th} = E_{th}/E_{max}$. By fitting Equation 2.13, ω_a can be extracted. An sample of data adhering to Equation 2.13 is shown in Figure 2·4.

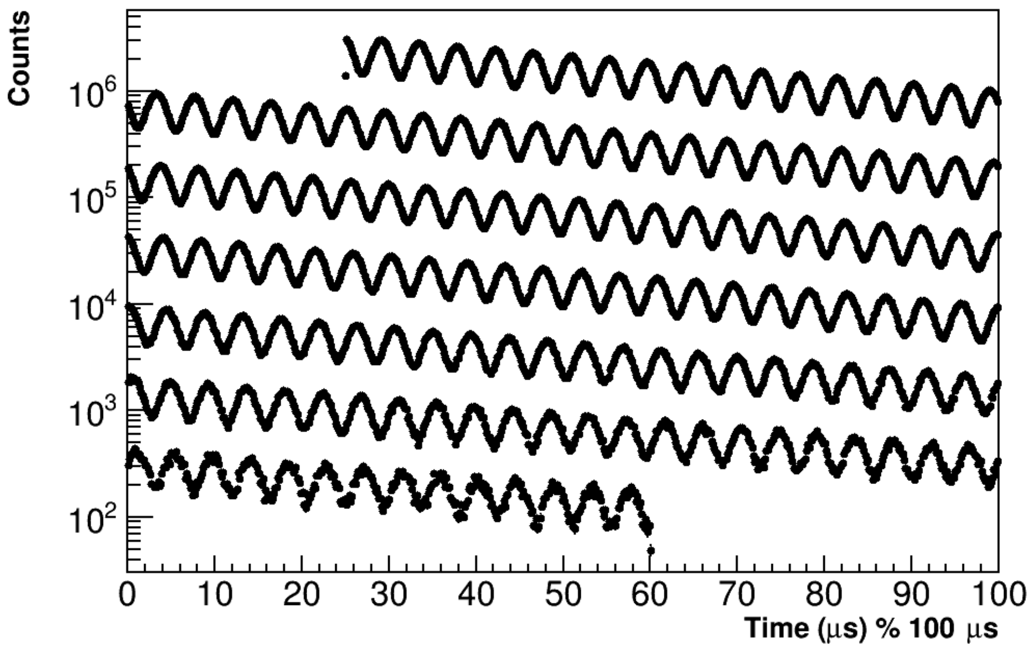

Figure 2·4: The number of detected positrons above some energy threshold ($y \sim 0.55$) as a function of time. The time axis is wrapped around every 100 μs.

2.2 Measuring the magnetic field

In order to measure the magnetic moment of the muon to 140 ppb, the field needs to be both highly uniform, and measured to extreme precision. The E989 goal for the field measurement is 70 ppb. As shown in Equation 2.6 the measurement of the magnetic field has equal weight to that of the precession frequency. A cross-section of the magnetic ring is shown in Figure 2·5. The muons live within a $9\,\mathrm{cm}^2$ storage region at the center of the magnetic field. This corresponds to an approximately $1.14\,\mathrm{m}^3$ or $40\,\mathrm{ft}^3$ total volume around the inside of the ring. The magnetic field is made uniform by manipulating many magnetic 'knobs' built into the $g-2$ storage ring, including the main magnet current, pole pieces, wedges, top hats, and thousands of small magnetic shims placed around the storage region. There is also an active feedback system which stabilizes the magnetic field over time. The shimming of the field to high precision, approximately ± 25 ppm, was a long process of fine tuning over the course of many months that was undertaken by many member of the field team.

Measuring the magnetic field comes down to measuring ω_p as shown in Equation 2.4. This is because the magnetic field measurement is made using a pulsed nuclear magnetic resonance technique (NMR). NMR was chosen as it provides a field measurement precision on the order of 10 ppb with negligible statistical uncertainty [27]. NMR probes work by rotating the magnetization of a sample of protons in some fluid, typically water or petroleum jelly, and then measuring the relaxation time or free-induction decay (FID) signal of the proton spins. The magnetization of the protons will relax back to equilibrium with the external field as the spins of the protons precess at the Larmor frequency and interact with local magnetic field gradients or inhomogeneities. Pickup coils are located around the sample which both deliver the pulse to rotate the proton sample magnetization and measure the FID signal. An example of an FID signal is shown in Figure 2·6.

Technically, it is not solely ω_p that needs to be measured. What really matters is the average magnetic field that the muons see, or the time-averaged spatially-weighted magnetic field. The scheme devised to measure this is two-fold. First, the magnetic field in the storage region where the muons live is measured by a trolley which drives around the inside of the ring. This trolley holds 17 NMR probes and measures the field at approximately 6000 locations around the inside of the ring. Because however the trolley cannot be in the beam path when the muons are present in the ring, during data taking it is pulled out of the way and the field is instead measured by 378 fixed NMR probes located in the high magnetic field region, but just outside the storage region. The prescription is that the fixed probes measure the field at all times, the storage ring field is measured every few days by the trolley probes, and the two are interpolated. In this way the magnetic field can be mapped over time and over

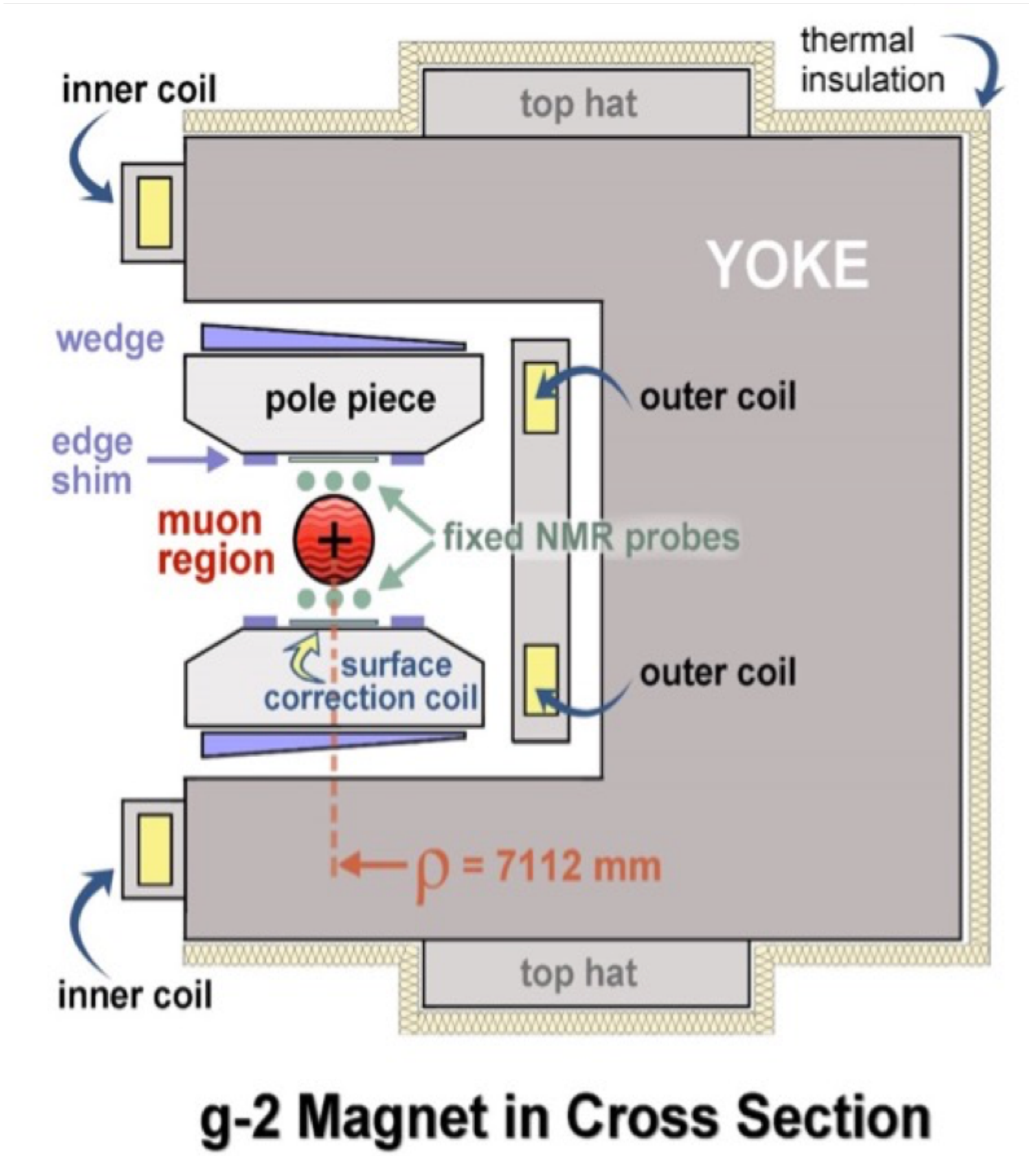

Figure 2·5: Cross-section of the $g-2$ magnet. The muons live in the storage region. This is surrounded by many magnetic features of the magnet which allow for sub ppm level tuning of the magnetic field.

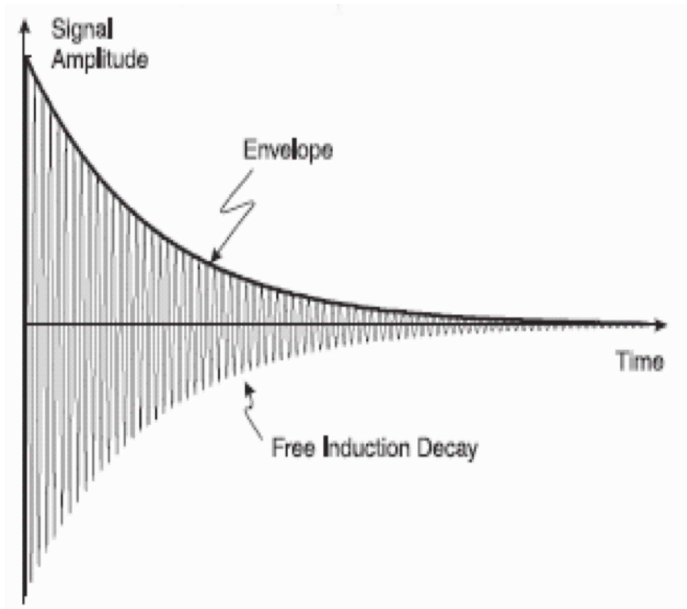

Figure 2·6: An example FID signal. The current picked up in the coils around the proton sample will oscillate as the spins precess around the main magnetic field, and decay as the spins return to alignment with the external field.

the space that the muons live in. A preliminary sample of the azimuthally-averaged magnetic field measured with trolley and fixed probes is shown in Figure 2·7. (Might want to find a better picture, and also figure out what the time averaging is.)

Lastly, it is the free proton precession frequency in the field that is of interest, but the frequency that the probes measure will be different due to the molecular properties of the proton sample as well as the material properties of the probe itself. The frequency that the probes measure can be re-casted as

$$\omega_{p,\mathrm{probe}} = \omega_{p,\mathrm{free}}(1 - \sigma(\mathrm{H_2O},\ \mathrm{T}) + \delta_b + \delta_p + \delta_s), \tag{2.16}$$

where $\sigma(\mathrm{H_2O},\ \mathrm{T})$ is the temperature dependent diamagnetic shielding of protons in a water molecule, and the δ's come from corrections due to the bulk susceptibility of the water sample, paramagnetic impurities in the water sample, and the magnetic effects of the probe itself, respectively [27]. In order to correct for these effects two additional

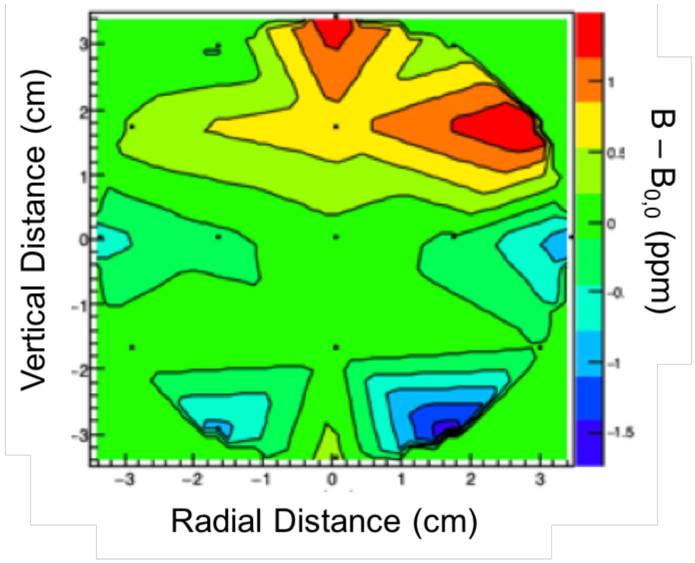

Figure 2·7: A sample of the azimuthally-averaged magnetic field within the storage region. The contours are normalized to the center value of the field. The scale of the field differences is approximately ± 1 ppm. The dots in the picture correspond to the location of the trolley probes.

special probes are used, both of which live in a single section of the ring which has been shimmed to extra uniformity. The first is a calibration probe which measures the free proton precession frequency at the center of the storage region corresponding to the placement of the central trolley probe. The calibration probe is made of materials in order to reduce the effects in Equation 2.16 and has been characterized in other test magnets. The second special probe is called the 'plunging probe.' This probe drops into the vacuum chamber and measures the field at each of the 17 trolley probe locations, using a three dimensional motion system. By using these two probes, the calibration for the free proton precession frequency can be transmitted to each of the trolley probes, providing for the needed measurement inside the storage region of the magnetic field. This calibration procedure is estimated to take up about half of the target systematic uncertainty of 70 ppb at 35 ppb, and is carried out every few days.

Other pieces of the systematic uncertainty include the absolute calibration of the calibration probe, the trolley measurements, the interpolation to the fixed probes, the uncertainty relative to the muon distribution, and others such as time dependent external magnetic fields. (Include table here? Page 437 in TDR.) When all is said and done, the measurement of the magnetic field is a complex and continuous process that is done in parallel to the measurement of ω_a throughout data taking.

2.3 Production and injection of polarized muons

As explained previously, the number of high energy positrons detected depends on the muon spin at the time of decay. In order for this detected quantity to mean anything, the muon spins themselves need to be highly polarized. Using the same parity-violation and spin momentum conservation logic as expounded upon in muon decay, it is known that pion decay produces muons that are 100% polarized in the pion rest frame, due to the pion having zero spin. The Feynman diagram for this decay is shown in Figure 2·1b. It's also important to note that pions decay to muons with over 99% branching ratio due to the parity violating nature of the weak interaction. These two facets of pion decay are used to construct polarized muon beams.

In order to measure $g-2$ to high precision, a very large number of positrons need to be detected, and hence a large number of highly polarized muons injected into the storage ring. The BNL E821 experiment observed on the order of 10 billion positrons above threshold, and its final result was statistics limited. In order to reach the goal of 140 ppb, 20 times that number of statistics needs to be gathered. The only facility in the world that can produce such a high number of polarized muons is Fermilab.

The Fermilab accelerator complex produces polarized muons for E989 in a number of stages. A map of the various relevant accelerator beam-line components is shown in Figure 2·8. Details of the full accelerator production of polarized muons can be found in Reference [28], and here will be given a summary of the process. Protons are first generated and accelerated in a linear accelerator called the "linac". They are

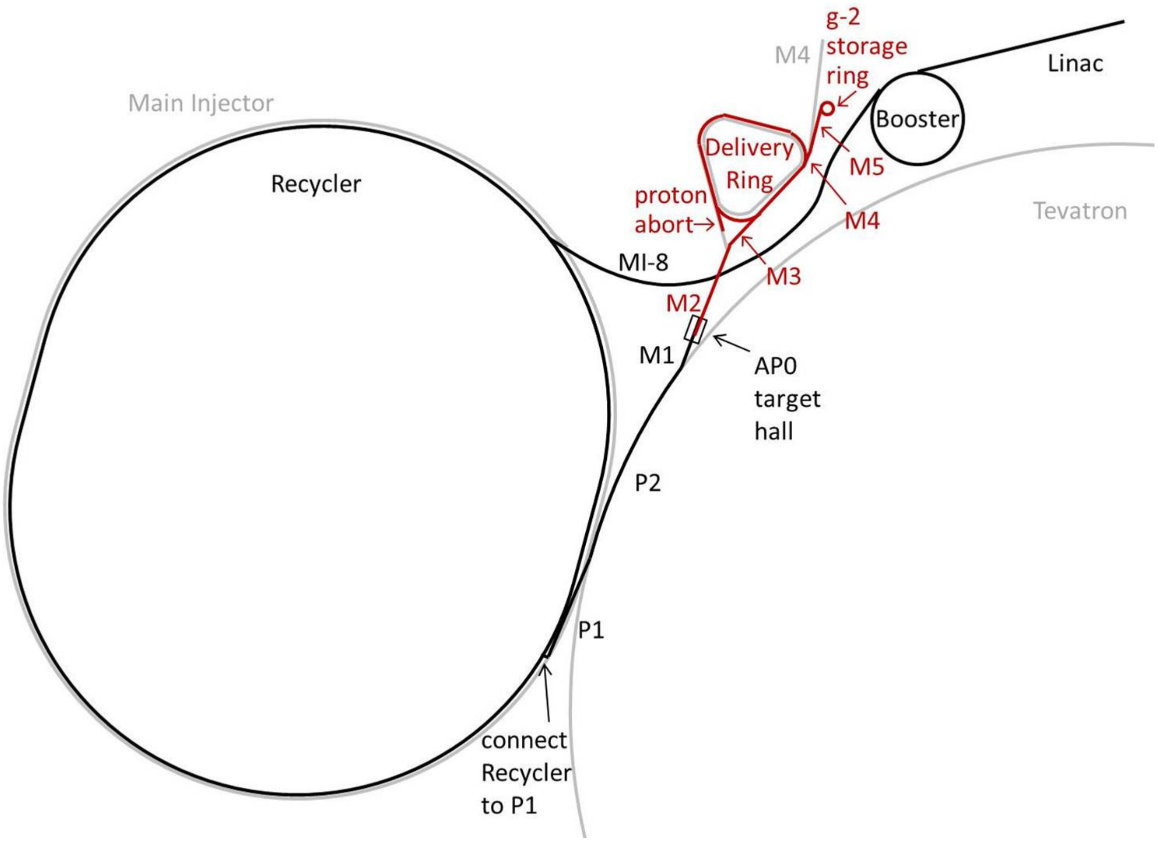

Figure 2·8: Plotted is the layout of accelerator beam-line components Fermilab uses to provide polarized muons to E989. Protons start in the Linac, traverse around the Booster and then Recycler, and are converted to pions at AP0. The pions are gathered and then decay away to muons in the Delivery Ring before being sent to the $g-2$ storage ring. Figure taken from Reference [27].

transported to a small circular ring called the “booster”, which accelerates them up to 8 GeV and puts them into a bunched structure. A single booster batch contains on the order of 4×10^{12} protons, which is too much for the detector data acquisition systems to handle at the data taking side of things. Therefore the protons are injected into a ring called “recycler”, which re-bunches the protons into four separate bunches of 1×10^{12} protons each, with a time width of approximately 120 ns. These bunches are delivered at a rate of about 12 Hz with a time separation of greater than 10 ms, again owing to the acceptable rates of the $g - 2$ detectors.

Each bunch is selected one at a time and sent to a target hall, where the bunch is smashed against an Inconel target. This Inconel target is made up of a nickel and iron alloy optimized for producing a large number of pions with a small momentum spread, approximately $1 \times 10^{-5}\,\pi^+$/POT with $|dp/p| < 2\%$ [28]. The resulting pions are focused just after production by a lithium lens. This lithium lens is a 1 cm radius and 15 cm long piece of aluminum which provides a radial focusing effect for particles passing lengthwise down the cylinder [29]. A pulsed magnet just after the lithium lens is then used to select pions at 3.115 GeV.

The pion beam and any residual protons are then injected into another ring called the “delivery ring”, which is used to hold the pion beam until the vast majority of pions decay. The pions are held in the delivery ring for four turns, after which they have all decayed to muons [28]. In a pion beam the highest and lowest energy decay muons are polarized. Therefore forward emitted polarized muons are then momentum selected at 3.094 GeV with $\Delta p/p = 2\%$, and the remaining muons, protons, and other secondary particles are re-routed to a beam dump which reduces the contamination in the final polarized muon beam. This polarized muon beam is then sent to the $g-2$ building where it passes through four magnetic quadrupole focusing magnets before being injected into the storage ring.

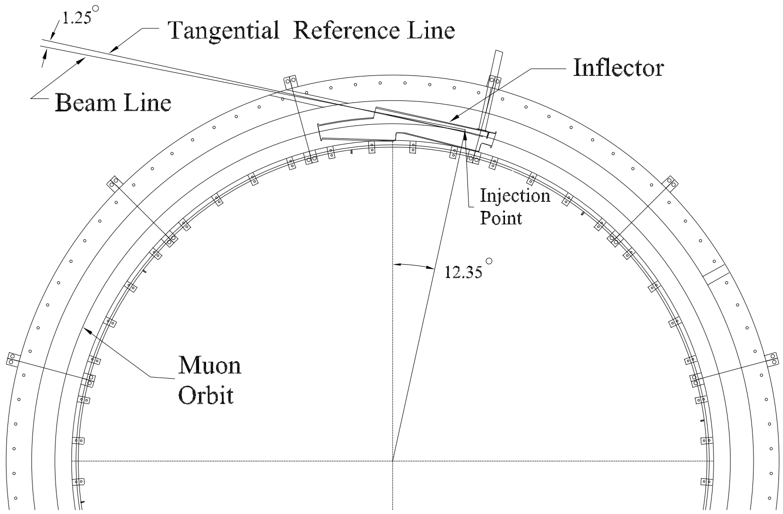

Figure 2·9: Shown is a birds eye view of the inflector and injection point into the storage ring.

The injection of the muon beam into the $g-2$ storage ring is a specialized process. In order to measure the magnetic field to the precision described in Section **??**, the $g-2$ storage ring must be a single monolithic magnet with no end effects. This prohibits the usual design of separated magnetic elements through which the muons might be injected. Therefore we use a specialized magnet called the "Superconducting Inflector" magnet, or just inflector. This inflector is placed within a bored out tunnel in the storage ring magnet, and it cancels the majority of the magnetic field of the storage ring at the injection point of the muons, such that they are not lost due to motion induced by the fringe field [30]. See Figure 2·9 for a view of the injection point. The inflector has a very tight 18 mm wide by 56 mm high aperture through which the muons must pass down its 1.7 m length. One side of the inflector is also closed such that an appreciable fraction of muons are lost before being injected into the ring, see Figure 2·10. Approximately 2% of injected muons are stored with $\Delta p/p = 0.5\%$ centered around 3.094 GeV due to these factors.

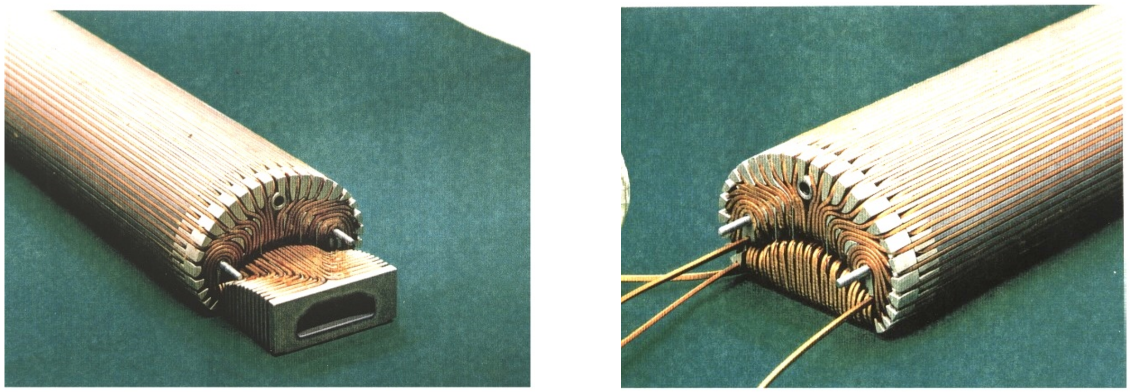

(a) Open end of the inflector.

(b) Closed end of the inflector.

Figure 2·10: Shown are the two ends of the inflector magnet. Superconducting coils are wrapped around a blank core in a complicated fashion which serves to eliminate the majority of external fields and shield the muons passing through it. One side of the inflector magnet is closed which causes an appreciable fraction of muons to be lost due to multiple scattering.

2.4 Storage of muons

The E989 experiment and storage ring are shown in Figure 2·11. Approximately 10,000 muons are stored in the $g-2$ ring at a time, corresponding to a single fill. The 3.094 GeV muons will decay with a lifetime of approximately 64.4 µs. Once the muons have been injected into the ring, they will begin orbitting clockwise around the ring. By necessity, the inflector must be out of the muon beam path, otherwise a large fraction of the muons would be lost upon the first return to the injection point. Therefore the muon beam must be manipulated to switch the orbit path from the injection orbit onto the central orbit around the center of the storage ring. Once the muon beam is centered, it must also be focused vertically, otherwise all of the muons would be lost due to any vertical motion of the muons. To perform the former, a magnetic "kicker" is used to shift the orbits of the muons. To perform the latter, a serious of electrostatic quadrupoles focus the beam vertically.

The "kicker" is made up of three separate pulsed magnets located 90° from the

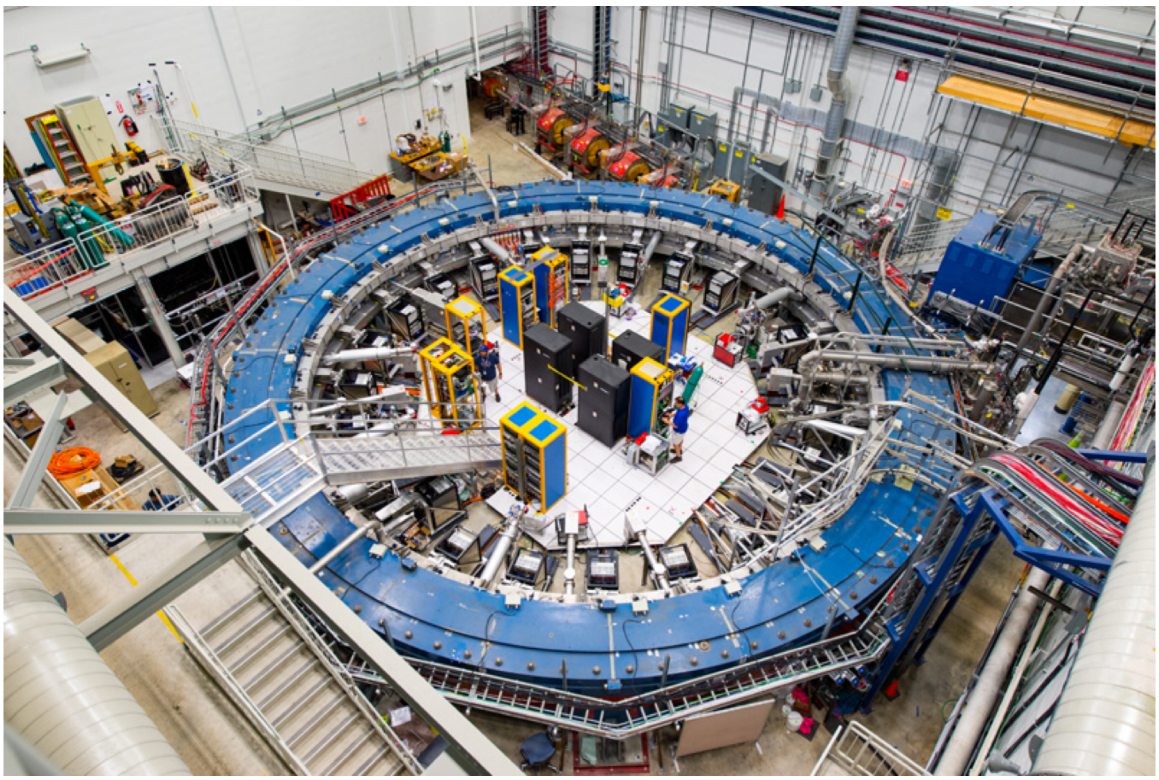

Figure 2·11: Shown is a picture of the $g - 2$ experiment. The blue painted storage ring can be seen to surround a variety of detectors and electronic. Muons come in at the top of the picture through a serious of magnetic quadrupoles from the accelerator and are injected into the ring, where they orbit in a clockwise direction. There are some people located inside the ring which gives a sense of scale to the picture.

exit of the inflector, where the inflector orbit crosses the central orbit. This is shown in Figure 2·12. Due to the bunched nature of the muon beam and the short cyclotron period of 149 ns, ideally the kicker moves all stored muons onto the central orbit and then turns off quickly such that by the time the muons orbit back around to the kicker there is no residual kick to the beam. The kick to the beam is approximately 10 mrad using a vertical pulsed field of around 300 Gauss over three 1.27 m long magnets and with a pulse length of about 120 ns. (Should I mention the actual kick here, and how the beam is not quite centered in the ring?) It's important to note that the kicker must be operated within the magnetic field of the ring, and must therefore contain no magnetic elements in the hardware itself which would perturb the uniform magnetic field. For this reason the kicker is made up of thin aluminum plates which carry the current used to create the kicking magnetic field.

There are four electrostatic quadrupoles (quads) located around the ring as shown in Figure 2·12, which focus the beam vertically and defocus the beam horizontally. (The magnetic field of the ring serves to restore the beam radially.) The strength of the electrostatic focusing can be characterized by the field index

$$n = \frac{\kappa R_0}{\beta B_0}, \tag{2.17}$$

where κ is the electric quadrupole gradient, B_0 is the magnetic field strength, R_0 is the central storage ring radius, and β is the relativistic velocity of the muon beam. Just as in the case of the kickers, the quads must be operated in the vacuum and must be non-magnetic. The latter is the reason why we use electrostatic focusing elements instead of magnetic ones in the first place. Four quads were chosen in order to maximize the symmetry of the beam motion around the ring. The quads occupy over 40% of the ring circumference. Each quad is made up of two segments, a short segment of 13° and a long segment of 26°. The quads are made out of as little material

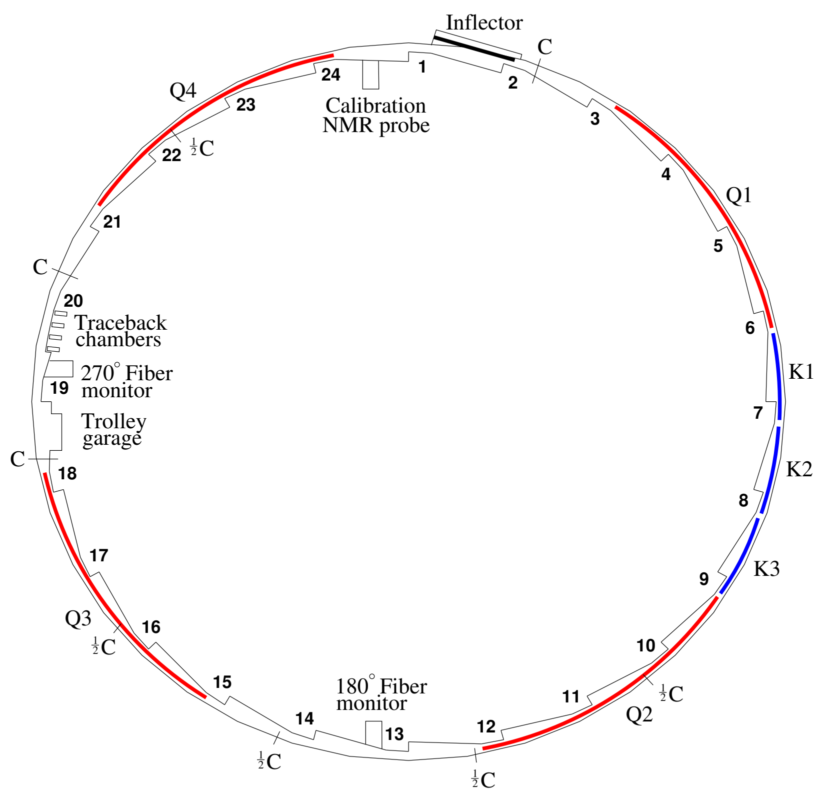

Figure 2·12: A map of the vacuum chambers in E989. K1-K3 show the locations of the kicker magnets, while Q1-Q4 show the locations of the electrostatic quadrupoles. Also shown is the location of the inflector, the two fiber monitors, and one of the tracker stations.

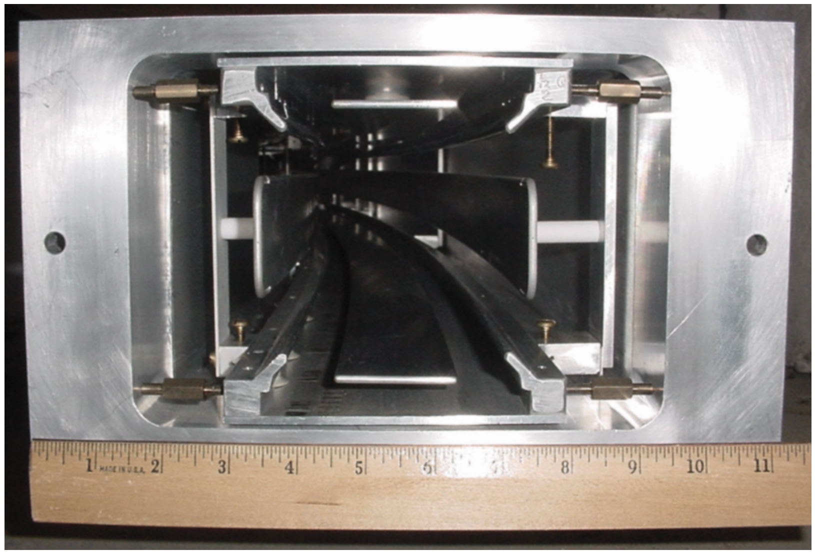

Figure 2·13: Electrostatic quadrupoles installed into a vacuum chamber. There are four plates mounted to the chamber through insulator standoffs. Also shown are the rails that the magnetic field trolley rides on around the inside of the ring, and between the quad and kicker plates.

as possible in order to reduce multiple scattering of decay positrons passing through them. A picture of the quads installed into one of the vacuum chambers is shown in Figure 2·13. The equipotential lines of the quads is shown in Figure 2·14.

As the muon beam goes around the ring, the muons will experience local field gradients and inhomogeneities. In order to avoid resonances where muons are lost from having passed through such regions too many times, the quad voltages are chosen such that the betatron wavelengths of the radial and vertical motions are not integer multiples of the storage ring circumference. This was one of the reasons that quadrupole voltages of 18.3 and 20.4 kV were used during Run 1 data taking. (Here is the first time I mention Run 1 data taking I think which doesn't make a ton of sense. Also should I go through all the tune stuff here? Or somewhere else? How much detail?)

Muons will be lost during data taking that will throw off the measurement of the

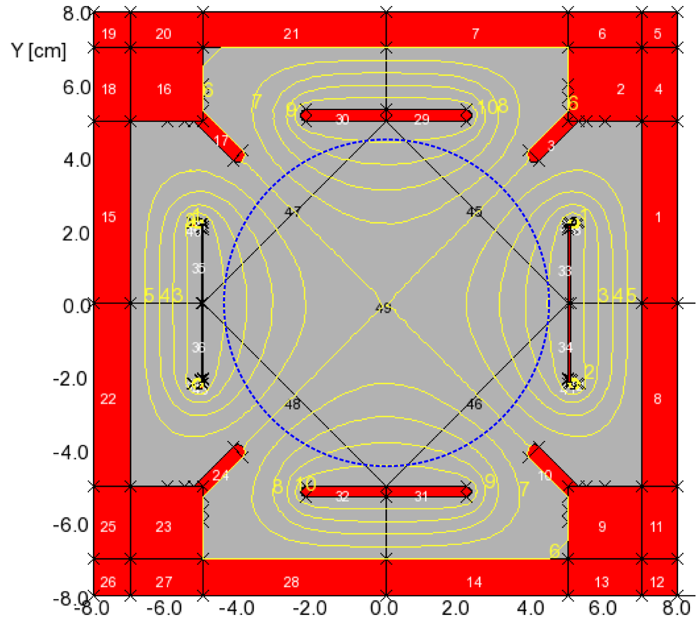

Figure 2·14: An OPERA model of the quads and their equipotential contours. The top and bottom plates sit at positive voltage while the left and right plates are at negative voltage. The muon storage region is shown by the blue circle. Picture from Reference [27].

precession frequency ω_a. In order to reduce the number of lost muons over the course of a fill, a procedure called "scraping" is used to remove those muons sitting at the edge of the storage region that will likely be lost at later times anyways. This scraping procedure involves changing the quad voltages in an asymmetric way such that the beam is pushed to the outside of the storage region, where the edges of the beam will impact copper rings called collimators. Muons which hit the collimators will lose energy and be lost as the muons spiral out of the ring. The scraping procedure is performed early in the fill and ends at something20 µs. During Run 1 it was discovered that some of the quad resistors were damaged, leading to longer RC time constants such that the quad voltages had not returned to storage nominal during the designated analysis portion of the data. (Show a picture here of those time constants?)

Muon Beam Frequencies		
Name	Frequency (MHz)	Period
$g-2$	0.23	4.365 µs
cyclotron	6.71	149 ns
coherent betatron	0.37	2.703 µs
vertical betatron	2.19	457 ns
vertical waist	2.31	433 ns

Table 2.1: Table of frequencies and corresponding periods seen in the $g-2$ experiment due to beam motion. Parameter values are from a subset of Run 1 corresponding to an n value of 0.108 or a quad voltage of 18.3 kV.

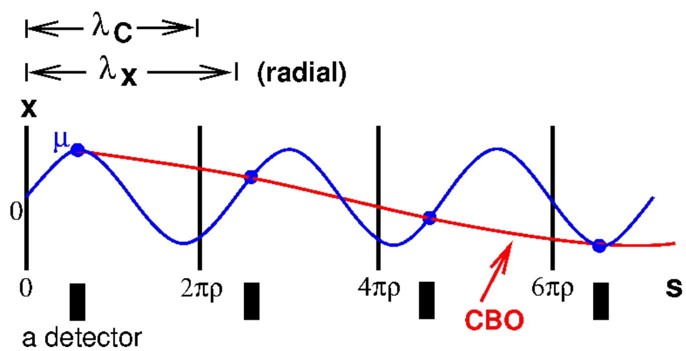

Figure 2·15

2.5 Muon beam motion

Due to the momentum and position spread of the injected muons, as well as the

2.5.1 Coherent betatron oscillation

2.6 Corrections to ω_a

Equation 2.3 is an idealized version of the spin difference frequency. Including practical experimental concerns, there are two corrections that must be applied to ω_a.

2.6.1 Electric field correction

In the presence of an electric field, the spin difference frequency is altered to

$$\vec{\omega}_a = -\frac{q}{m}[a\vec{B} - \left(a - \frac{1}{\gamma^2 - 1}\right)(\vec{\beta} \times \vec{E})], \tag{2.18}$$

where now there is an extra term dependent on the electric field strength and the momentum of the particles. This is necessary to include since we use electrostatic quadrupoles for vertical focusing as described above. The second term cancels to first order for a specific momentum or value of γ. This "magic momentum" can be understood as the momentum at which a relativistic particle moving through an electric field has its spin exactly follow its momentum. This magic momentum is 3.094 GeV for muons, hence the momentum value of the injected muons. This value has driven many of the design constraints of the $g-2$ experiment, including the size of the storage ring, choice of the magnetic field magnitude, and so on.

Not all muons will have the magic momentum however as described in the inflector section Section **??**, and therefore a correction to the measured ω_a frequency needs to be applied. Approximating the storage ring as having an electric field applied over the whole azimuth of the ring, the spin difference frequency for muons with momentum $p \neq p_m$ (where p_m is the magic momentum) becomes

$$\omega_a' = \omega_a\left[1 - \beta\frac{E_r}{cB_y}\left(1 - \frac{1}{a\beta^2\gamma^2}\right)\right]. \tag{2.19}$$

Here the motion of the beam is assumed purely azimuthal. This additional term is the electric field correction that then serves to lower the measured ω_a frequency. Using the relation $p = \beta\gamma m = (p_m + \Delta p)$, after a little bit of simplification the electric field correction can be written as

$$C_{\mathrm{E}} = \frac{\Delta\omega_a}{\omega_a} = -2\frac{\beta E_r}{cB_y}\frac{\Delta p}{p_m}. \tag{2.20}$$

The last fraction can be related to the field index described in Equation 2.17 by

$$\frac{\Delta p}{p_m} = (1-n)\frac{\Delta R}{R_0} = (1-n)\frac{x_e}{R_0}, \tag{2.21}$$

since we know that the magic momentum muons live at the center of the storage ring radius R_0. In this equation $x_e = \Delta R$ is the equilibrium radius of the beam relative to the central storage radius. Noting that the electric field strength is

$$E = \kappa x = \frac{n\beta c B_y}{R_0} x, \tag{2.22}$$

and assuming that it is perfectly radial, the electric field correction can be reduced to

$$C_{\mathrm{E}} = -2n(1-n)\beta^2 \frac{x x_e}{R_0^2}. \tag{2.23}$$

Taking the time average of the beam motion, where x is simply equal to x_e, then the correction becomes

$$C_{\mathrm{E}} = -2n(1-n)\beta^2 \frac{\langle x_e^2 \rangle}{R_0^2}. \tag{2.24}$$

This electric field correction can be determined through analysis which relates the beam momentum to the equilbrium radius. (Should expand on that somehow here.) The assumptions made here are sufficient for the $g-2$ measurement [**something**]. (Cite something here or actually derive something?)

2.6.2 Pitch correction

Particles injected into the $g-2$ storage ring will have some motion component that is vertical, or parallel to the magnetic field vector (hence the need for vertically focusing electrostatic quadrupoles). This will reduce the magnetic field seen by the muons in their rest frame slightly. Including this motion into the spin difference frequency

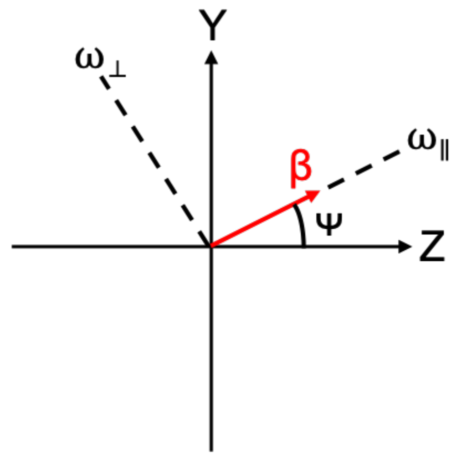

Figure 2·16: Beam motion β relative to the vertical and azimuthal axes Y and Z respectively. ψ is the pitch angle of the beam, and the dashed lines represent the parallel and perpendicular motions of the beam.

(along with the electric field correction describe previously), ω_a becomes

$$\vec{\omega}_a = -\frac{q}{m}[a\vec{B} - a\Big(\frac{\gamma}{\gamma+1}\Big)(\vec{\beta}\cdot\vec{B})\vec{B} - \Big(a - \frac{1}{\gamma^2-1}\Big)(\vec{\beta}\times\vec{E})], \tag{2.25}$$

where now there is an extra term in the middle dependent on the vertical betatron motion of the beam. Similar to the electric field case, this term can be neglected to first order as the muon momentum is nearly all perpendicular to the field, but a correction again needs to be applied to ω_a to account for this effect.

Since the muons in the storage ring will be oscillating vertically as they are focused by the quads, their momentum vectors will be pitching up and down relative to the azimuthal motion. This pitch angle will oscillate as

$$\psi = \psi_0 \cos(\omega_y t), \tag{2.26}$$

where ψ_0 is the amplitude of the oscillation and ω_y is the vertical betatron frequency. Shown in Figure 2·16 is an exaggerated example of the beam motion relative to the vertical and azimuthal axes. Assuming that the field is purely vertical, $\vec{B} = B_y\hat{y}$ and that the beam motion is in the vertical-azimuthal plane,

$$\vec{\beta} = \beta_y \hat{y} + \beta_z \hat{z} = \beta \cos(\psi)\hat{y} + \beta \sin(\psi)\hat{z}, \tag{2.27}$$

then ω_a becomes

$$\vec{\omega}_a = -\frac{q}{m}[aB_y\hat{y} - a\Big(\frac{\gamma}{\gamma+1}\Big)\beta_y B_y(\beta\cos(\psi)\hat{y} + \beta\sin(\psi)\hat{z})], \tag{2.28}$$

where in this case the electric field part has been ignored. Using the small angle approximation such that $\cos(\psi) \approx 1$ and $\sin(\psi) \approx \psi$, $\vec{\omega}_a$ can be separated into its vertical and azimuthal components

$$\omega_{ay} = \omega_a\Big[1 - \Big(\frac{\gamma-1}{\gamma}\Big)\psi^2\Big], \tag{2.29}$$

$$\omega_{az} = -\omega_a\Big(\frac{\gamma-1}{\gamma}\Big)\psi. \tag{2.30}$$

Looking at Figure 2·16 again, it can be seen that the spin difference frequency can be resolved into its parallel and perpendicular components $\omega_\parallel$ and $\omega_\perp$ respectively. As the pitch angle of the beam motion oscillates about the azimuthal axes at a frequency much greater than the $g-2$ frequency, it can be seen that the parallel component averages to 0 over time. (Haven't given a number for the vertical betatron frequency yet.) We then only care about the perpendicular oscillation of the beam, which can be determined with a simple rotation matrix such that

$$\omega_a \approx \omega_\perp = \omega_{ay}\cos(\psi) - \omega_{az}\sin(\psi) \approx \omega_a\Big[1 - \frac{\psi^2}{2}\Big], \tag{2.31}$$

where in the last approximation the small angle approximation was used once again, but this time with $\cos(\psi) \approx 1 - \psi^2/2$. The pitch correction then is the additional term which serves to lower the measured spin difference frequency. Taking the time average,

$$C_{\mathrm{P}} = \frac{\Delta\omega_a}{\omega_a} = -\frac{\langle\psi^2\rangle}{2} = -\frac{\langle\psi_0^2\rangle}{4}, \tag{2.32}$$

where Equation 2.26 was used in the last equality. The pitch angle of the beam cannot be measured directly, however we know from Equation **??** or Section **??** that the angle of the beam can be related to the vertical distribution of the beam, such that

$$C_{\mathrm{P}} = -\frac{n}{4}\frac{\langle y^2\rangle}{R_0^2}. \tag{2.33}$$

Once again n is the field index, R_0 is the radius of the ring at the center of the storage region, and $\langle y^2\rangle$ is the vertical width of the beam. The first two are known and the last can be measured experimentally. (For this last equation make sure that what I write here gels with what I'll put in other sections, which haven't been done yet.) While this derivation was an approximation assuming continuous quads around the ring, it suffices for the level of precision necessary for the $g-2$ experiment [**something**].

Need to included beam motion and coherent betatron oscillations somehow I think in this chapter

Chapter 3

Detector Systems

-how should I order these sections? perhaps by what the beam sees in order?

3.0.1 T0

In order to align the decay positron spectra in time from fill to fill, an entrace "T0" detector is used. It is made up of a scintillating paddle connected to two (2-inch Hammatsu?) PMTs (photo-multiplier tubes), and is placed just on the outside of the ring before the inflector. See Figure 3·1. One of the PMTs serves as the actual T0 counter which provides an average time of the incoming beam with which to align the fills. The second paddle acts as a magnitude counter to serve as a proxy for the fill intensity. Together they provide a measure of the injected beam profile in time. The varying intensity and bunch shapes can be seen as shown in Figure 3·2.

-might use the same WFD as Calo 1... -cite all this, with the TDR or hopefully something else [27] - can possibly just cite DocDBs as well - need to figure that out -double check all this - just wrote from memory, also add detail - might want to just explain things better too, "one PMT with low pe stats and one with high pe stats" and how that works in the way I've already described above - ND (neutral density filters) one at 1% one at 10% -if I use p.e. include it in the abbreviations -get a picture of a T0 output from the midas page, also possibly comparing various bunches -docDB 10911 for details -docDB 10162 for pictures by Hannah

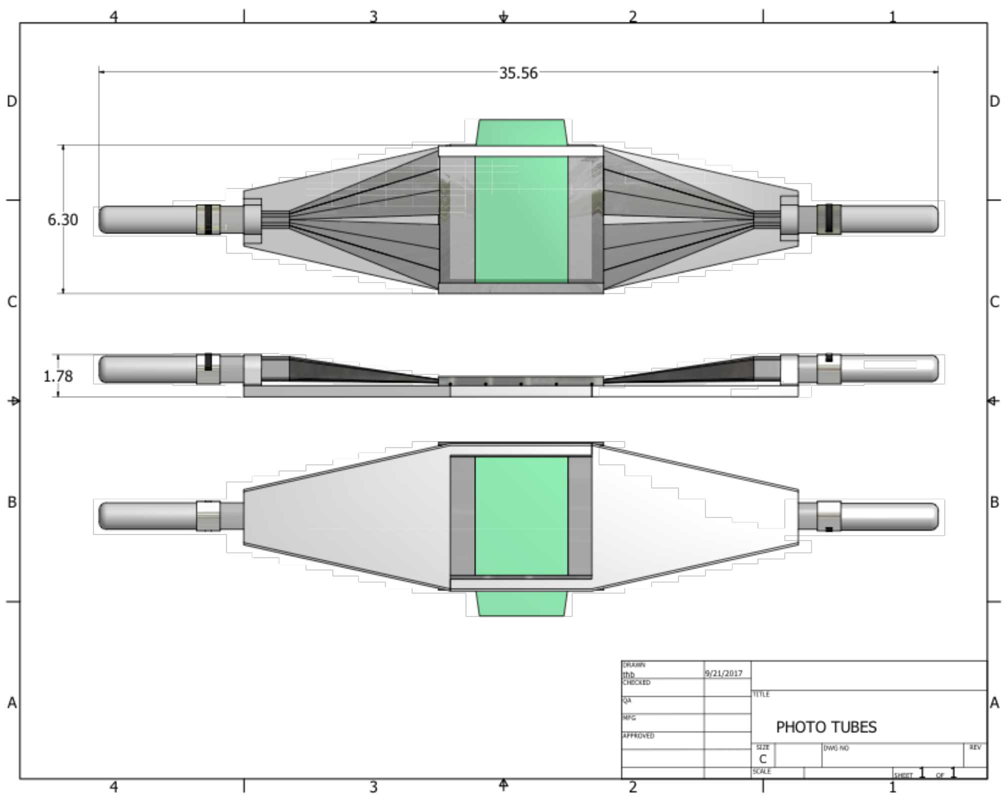

Figure 3·1: Shown is the T0 entrance counter. In the center in green is the scintillator, which connects with light guides to PMTs on the left and right. Each PMT has a separate ND (what's this?) filter to modify the light output into each PMT to configure one more for fill timing, and the other for fill intensity.

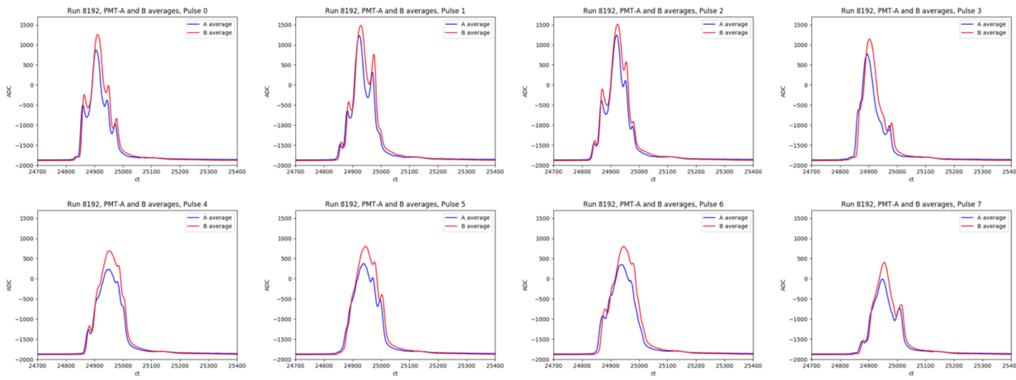

Figure 3·2: Shown are time profiles for the two PMTs (A and B) in the T0 counter for the 8 pulses we receive in an accelerator cycle/bunch/what. (careful here - not quite right) Each profile is an average of 100 such profiles. The x axis is in clock ticks (ct), each of which is 1.25 ns. (I will probably explain cts before this somewhere right?) PMT A is the low stats p.e. phototube and PMT B is the high stats p.e. phototube. Picture is too small, might want to rotate or replace it with somthing.

3.0.2 IBMS

There are two scintillating fiber detectors which monitor the beam as it passes through the inflector, the so-called inflector beam monitoring system (IBMS). See Figure 3·3. These devices are placed at the outside of the magnet yoke before injection into the back hole of the magnet, and at the entrance to the inflector. A third device is planned to be at or near the downstream end of the inflector (fix this later on). See Figure 3·4. These devices are used to verify the beam optics tune in the muon injection through the inflector and continuously diagnose beam properties as a handle on systematic problems. Probably cite something in this section - not the TDR since the IBMS was not included in the TDR.

-justification document - DocDB 2722 -DocDB 10944

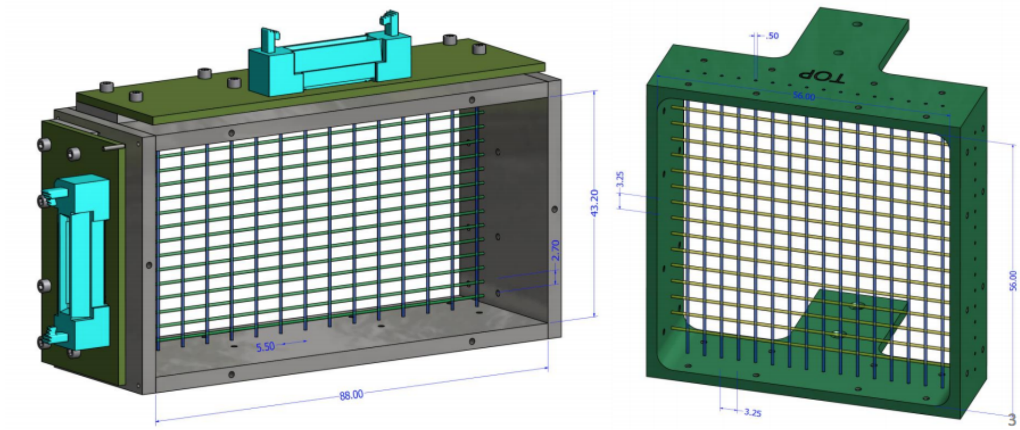

Figure 3·3: Simulation models of the IBMS 1 and 2 detectors. Scintillating fibers form an array which detect particles as they pass through them.

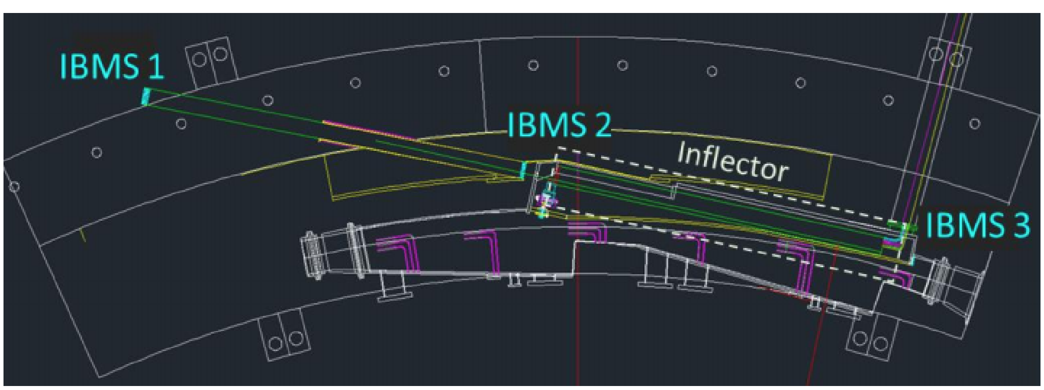

Figure 3·4: The positions of IBMS 1, 2, and the planned 3rd system are shown with respect to the vacuum chamber and inflector.

3.0.3 Fiber Harps

There are four scintillating fiber detectors located within the ring, two at the 180 degree position which measure the vertical and horizontal directions respectively, and similarly at the 270 degree position. One of these devices is shown in Figure 3·5. These 'fiber harps' serve to monitor beam properties at all times during a fill, including just after injection and during scraping. This is especially useful as a diagnostic tool as well as a measurement of the central beam position and CBO properties (have I talked about this yet?). Because the fiber harps are a distructive measurement of the beam, they are retractable and are only inserted in special runs in order to make said beam measurements. When they are inserted however they provide a wealth of useful information regarding the beam, as shown in Figure 3·6. Probably cite something in this section.

-DocDB 8366 -maybe find another docb/source

3.0.4 Calorimeters

Electromagnetic calorimeters measure the times and energies of decay positrons as they curl inward from the storage region. There are 24 calorimeters located symmetrically around the inside of the ring in close proximity to the vacuum chamber, as shown in Figure 3·7. They lie close to the storage region in order to measure a large fraction of the total number of observable decay positrons, including the high energy decay positrons which curl inward only slightly more than the muons themselves do. (max acceptance)

Each calorimeter consists of 54 channels of PbF_2 crystals arrayed in a 6 high by 9 wide array, which measure Cerenkov light emitted by the incident positrons as they pass through the crystals [31]. (Picture of single calo and its crystals here.) Cerenkov light is naturally fast which improves timing resolution of the incoming hits. Each

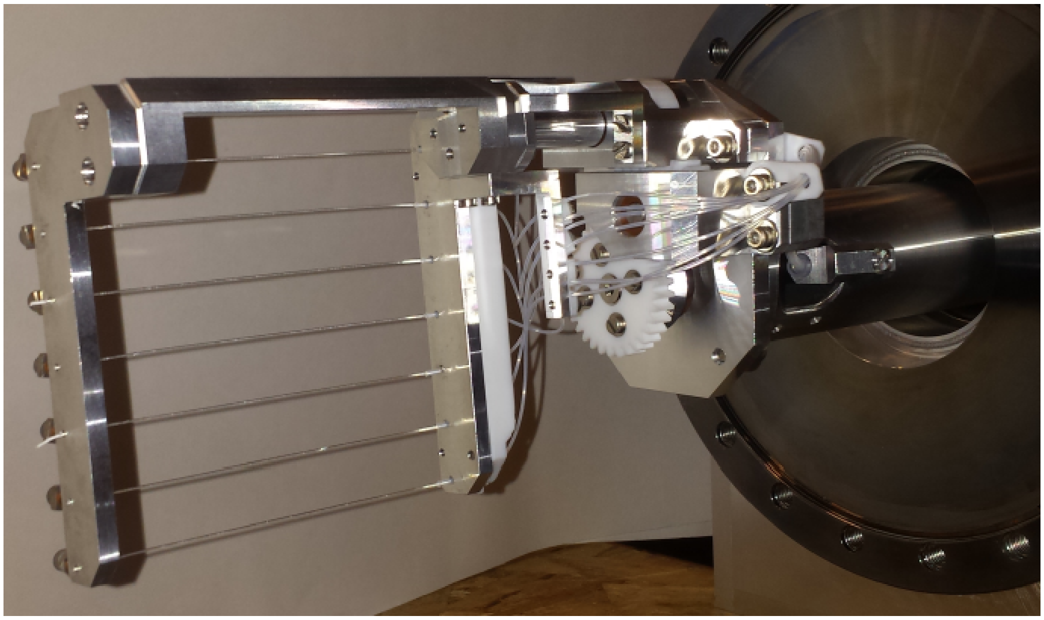

Figure 3·5: Picture of one of the fiber harps. A row of 7 scintillating fibers measures the beam instensity as a function of time at various vertical or horizontal components depending on which fiber harp is inserted.

crystal is 2.5 x 2.5 x 14 cm^3 and is wrapped in black Tedlar® foil to reduce light transmission between crystals and improve position reconstruction, as well as reduce pulse width [32]. The light is read out by large area silicon photo-multiplier (SiPM) sensors. Each calorimeter sits on a board extending out from a cart containing the electronic which power the calorimeters and read out the data, as shown in Figure **??** This is to relocate magnetic material away from the field region to avoid perturbing the field and to remove sensitive electronics from the decay path region. Similarly, due to the close proximity to the storage region and by extension the magnetic field, the calorimeters, the encapsulating material, and the SiPMs are made from non-magnetic material.

In order to determine a_μ to the precision goal, there are modest requirements on the performance of the calorimeters. They must have a relative energy resolution of better than 5% at 2 GeV, in order for proper event selection [27]. They must have

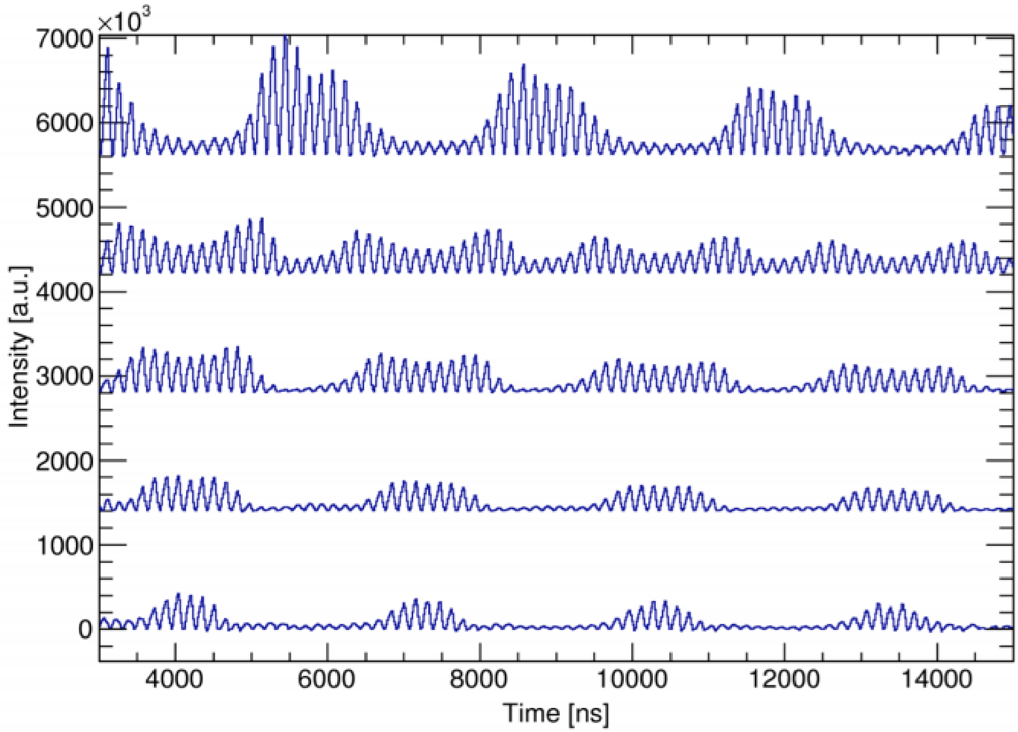

Figure 3·6: The fiber harps measure beam intensity as a function of time and fiber number. The middle spectrum is the output from the middle fiber, the upper spectra being fibers which are at successively greater radial positions, and the lower spectra being fibers which are at successively lower radial positions. The fast oscillations of the cyclotron frequency can be seen along with the slower oscillations of the CBO. This particular set of data was at a time or run when more beam was on the outside part of the storage region. (This last part is conjecture somewhat - maybe I should leave it out. I might honestly also want to leave out this whole picture, not sure..)

a timing resolution of better than 100 ps for positrons with greater than 100 MeV energy. The calorimeters must be able to resolve multiple incoming hits through temporal or spatial separation at 100% efficiency for time separations of greater than 5 ns in order to reduce the pileup systematic error due to the high rate. Finally, the gain of the measured hits must be stable to $< 0.1\%$ over a 200 μs time period within a fill, and unaffected by a pulse arriving in the same channel a few nanoseconds earlier. The long term gain stability over a time period of order seconds must be $< 1\%$. The SiPMs chosen satisfy these requirements (as well as the physical ones), due to their fast rise times and consistent pulse shapes. (Should this part be here? Or elsewhere? Before perhaps? Might need to update the gain numbers...)

(I've condensed quite a bit this section from the TDR - is that okay?)

A 12 bit waveform digitizer (WFD) samples each photodetector channel at a rate of 800 MSPS with a 1 Gb memory buffer and the data are transferred to a bank of GPU processors for on-line data processing [33]. The timing resolution of these WFDs is < 50 ps for most pulse amplitudes.

Should I go into the calorimeter DAQ here? Or make that it's own section - how uniform are the DAQ systems for each detector system? Are the same sorts of modules and crates and WFDs used or what? If so it's own section might make sense, otherwise probably include small pieces at the end of each individual detector about the daq system

3.0.5 Laser Calibration System

In order to satisfy the gain requirements, a laser calibration system was put into place in order to monitor the SiPM responses over short times (fill level), and long term (days to years). By comparing a known signal to the SiPM output. At the front face of each calorimeter is a board containing prisms connected to fibers from the laser system which can be pulsed in-fill or out of fill for each crystal individually.

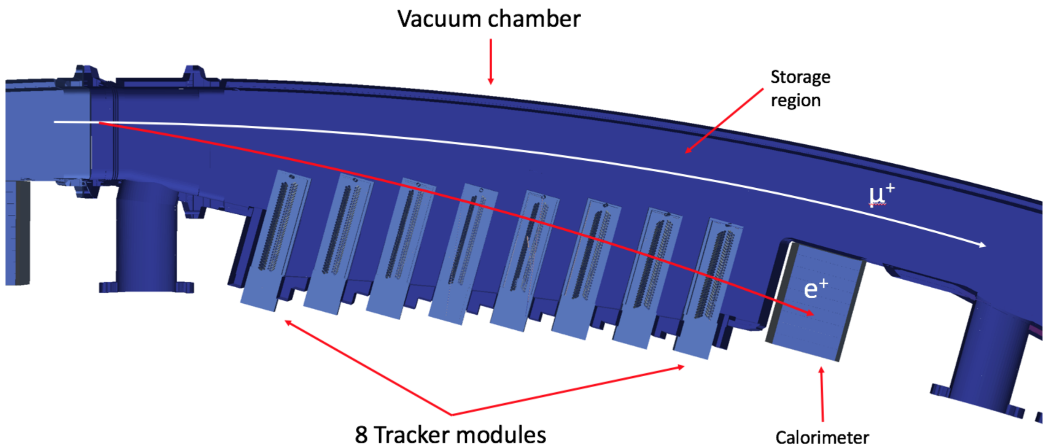

Figure 3·7: Birds eye view of a model of a vacuum chamber containing a tracker station, and the associated calorimeter. Muons pass around the ring in the center of the storage region which is contained within the bulk of the vacuum chamber. The muons decay to positrons, some of which then pass through the trackers or hit calorimeters. Each tracking station consists of 8 tracker modules.

-can pulse laser in fill, out of fill, and double pulse -mention the laser hut at all? probably not

[34] [35] [36]

3.0.6 Straw Trackers

The Muon $g-2$ Experiment at Fermilab uses straw tracking detectors to measure decay positron trajectories for the purpose of determining the muon beam distribution and its characteristics (and other things....). By fitting these tracks and extrapolating back to the average decay point, the beam can be characterized in a non-destructive fashion. See section blah. This is important because of the need for matching the average observed magnetic field of the decaying muons and their resulting decay positron directions which result in the ω_a frequency.

The trackers are also useful for determining general beam diagnostics as well as the pitch correction and to a lesser extent the electric field correction (careful here).

Cross-checking separately for pileup removal, hit verification, etc. is a powerful tool. Combining them in order to provide the muon distribution that the calorimeters directly see for the ω_a calculation is perhaps the most important role of the tracker. With three trackers, approximately 5% of decaying muons will result in measureable positron tracks assuming no pileup in the tracker, many of which do not hit the nearest calorimeter.

Each tracker module consists of 4 layers of 32 straws with a stereo angle of 7.5 degrees, the first two "U" layers oriented with the tops of the straws at a greater radial position, and the second two "V" layers oriented with the bottoms of the straws at a greater radial position. A tracking module is shown in Figure 3·8. There are 2 tracker stations located in front of calorimeters 13 and 19, or at approximately 180 and 270 degrees counting clockwise from the top most point of the ring where the inflector resides. Figure **??** shows this. (A third station sits empty after the inflector.) Each station consists of 8 tracking modules arranged in a staircase pattern that follows the curvature of the ring as seen in Figure 3·9.

In order to reduce the amount of multiple scattering within the straw tracking chambers as particles pass through them, the material of the straw trackers is minimized. Each straw is made of mylar foil, within which a 25 μm radius tungsten wire resides, and is filled with Argon-Ethane gas [**something**]. Fast moving particles ionize the gas as they pass through it, and the resulting ions are drawn to the wire which is held at high voltage. When they reach the wire (and the mylar) a signal can be read out which tells us that a particle was seen to pass through the straw. By combining many such signals in a brief time span, we are able to construct tracks of incidient particles. (See section blah.) The resolution of hits within the straws is approximately 150 μm [**something**].

The signals of the straws are read out through...

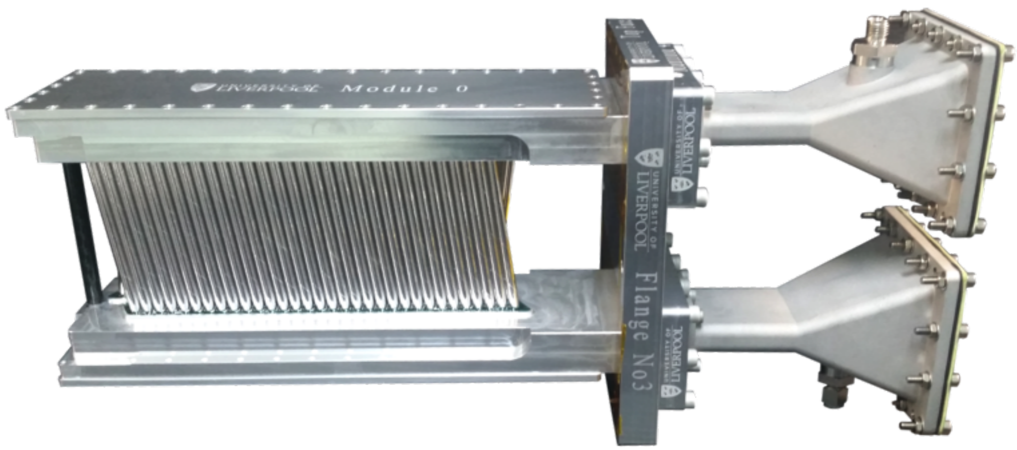

Figure 3·8: Shown is a picture of one of the many tracking modules used in the Muon $g - 2$ experiment. The first layer of straws with a stereo angle of 7.5 degrees can be seen, with the other 3 straw layers hiding behind it. The beam direction is roughly into the page in this picture, to the left of the end of the module, and this view is what the decay positrons will see.

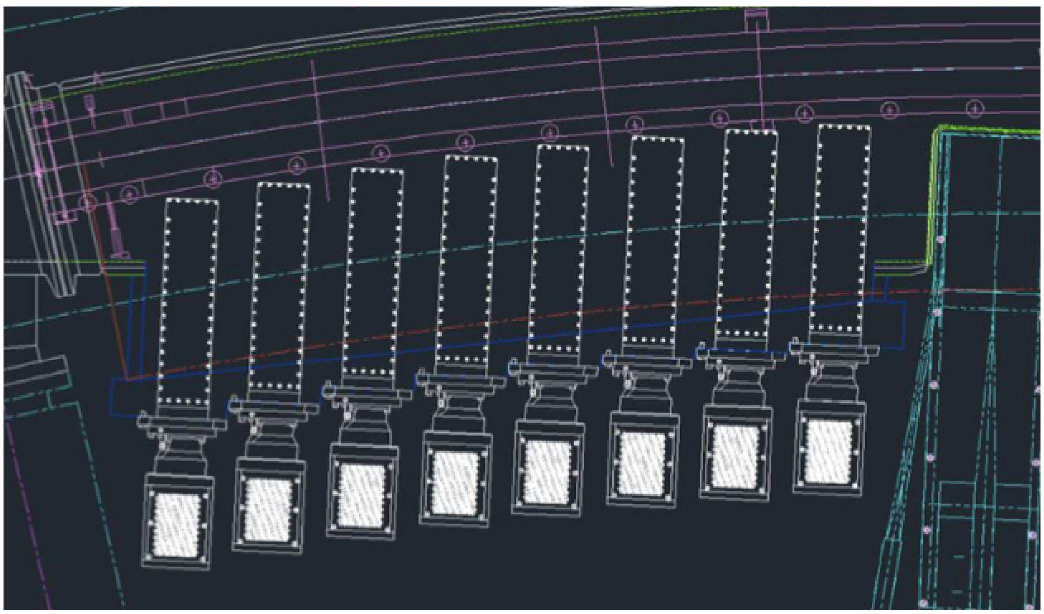

Figure 3·9: Tracker modules are arranged in the shown staircase pattern. In green and dark blue is the edge of the vacuum chamber (where the dark blue identifies the modification that was made to the old vacuum chambers), and it can be seen that vacuum chamber walls lie at the ends of the outside tracking modules. The position of a calorimeter can be seen in cyan at the right. The dark red spots are the locations of the outside magnet pole tips. From the shown geometry one can see that many positrons will hit either the tracker or the calorimeter but not both due to the acceptance differences.

Chapter 4

Straw Tracking Analysis

4.1 Straw Tracking Intro

As was talked about briefly in section 3.0.6, the straw trackers are used to provide information about the muon beam, as well as info for the calorimeters. The straw track reconstruction is performed in several stages. The “Track Finding” stage takes incoming hits and decides which hits should be grouped together to form a single track for a single positron. The “Track Fitting” stage fits the measured positions of these invididividual hits and forms a single track describing the trajectory of the incident positron. Finally the “Track Extrapolation” stage takes the fitted track information and extrapolates the position and momentum components to the regions of interest, namely the storage region and the calorimeter.

-see the previous section for the hardware information... -Geane (Geometry and Error Propagation)

4.2 Track Finding

4.3 Track Fitting

The Geane fitting routines originated in Fortran with the EMC collaboration, and was used in the precursor E821 experiment as well as the PANDA experiment with some success [37], [38]. (I’m not actually aware of a useful reference for it’s use in E821, and there are some other instances of its use as well in other experiments. In E821

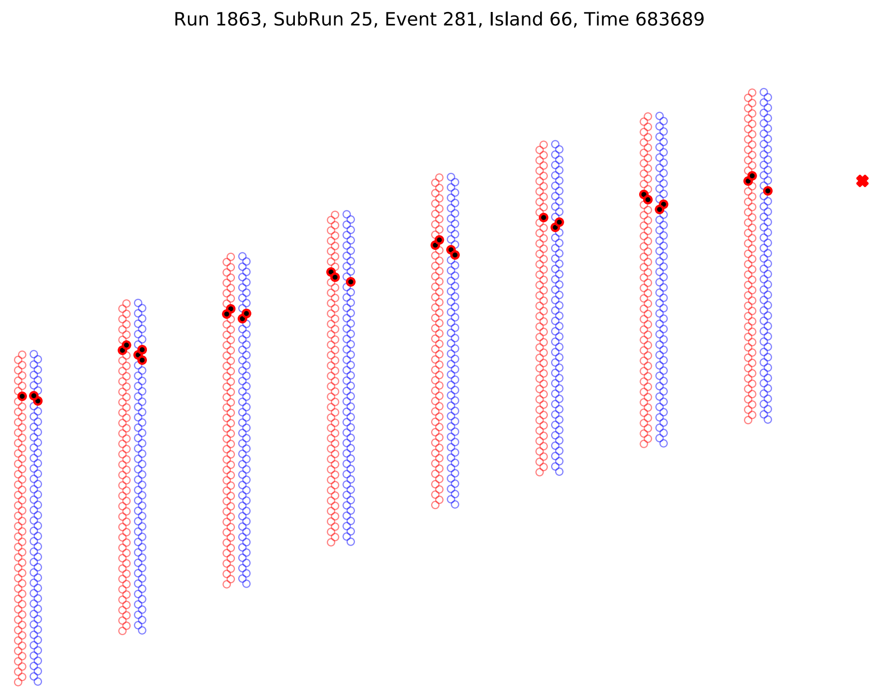

Figure 4·1: clean up and possibly replace

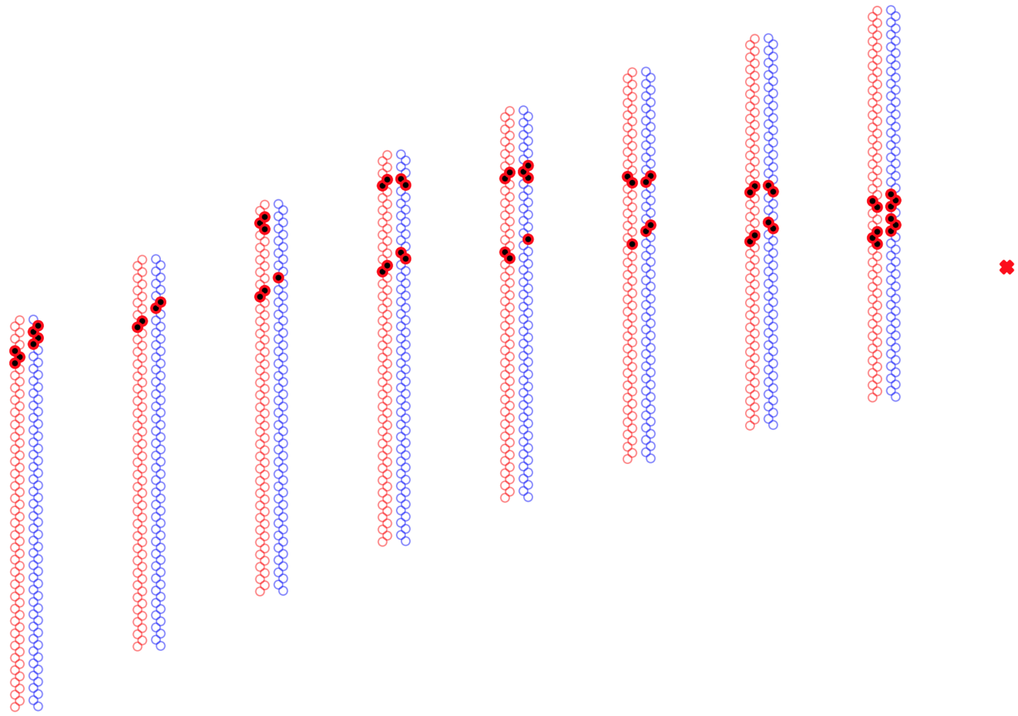

Figure 4·2: clean up and possibly replace

there was a single tracking chamber which was never put to full use.) The core error propagation routines were at some point added to Geant4 under the error_propagation directory which is included in all default installs. The tracking code strengths lie with its direct implementation and access to the Geant4 geometry and field, and its ability to handle the field inhomogeneties. The Geane fitting algorithm code which makes use of the Geant4 error propagation routines follows the structure of [37] and is detailed in the Formalism section in this paper. It is a relatively straight forward least squares global χ^2 minimization algorithm.

Because of the proximity of the trackers to the muon beam, they will lie within a region of varying magnetic field. The radial field of the trackers rises from 0 Tesla at the outer ends to roughly .3 Tesla at the inner top and bottom ends, and the vertical field drops approximately 50% from the storage dipole field of 1.451 Tesla. Shown in Figures 4·3 and 4·4 is the location of the tracker with respect to the horizontal

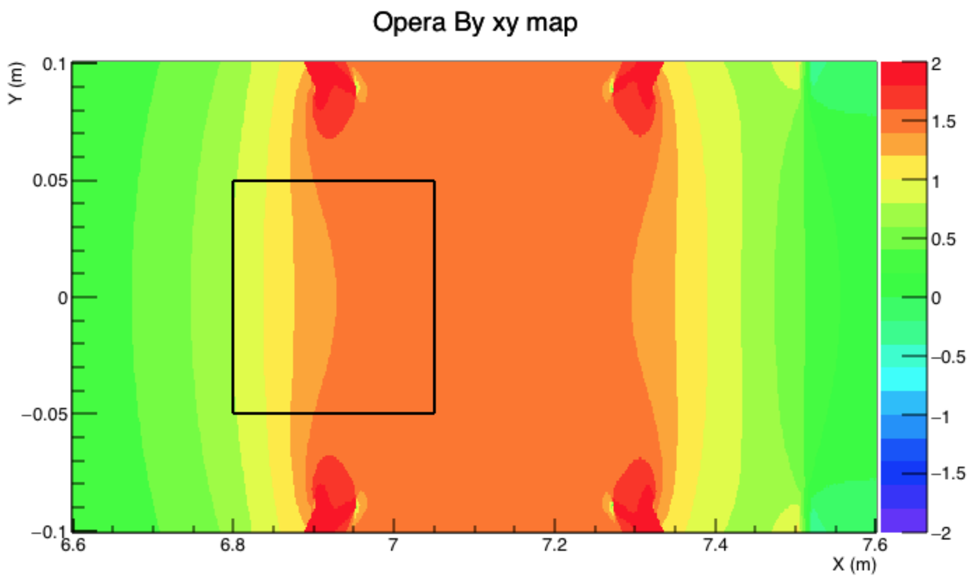

Figure 4·3: Shown is the vertical field of the $g-2$ magnet in and around the storage region as calculated in Opera 2D. The center of the storage region lies at 7.112 m along the x axis. The black box shows the rough location of the tracker with respect to the field (size exaggerated slightly). It can be seen that there is a large inhomogeneity within the tracker space, goring from left to right.

and vertical fields respectively. These large field gradients over the tracking detector region and the long extrapolation distance back to the muon decay point are special to Muon $g-2$. This is one of the main motivations for using the Geane fitting algorithm and routines, which has direct access to the field.

4.3.1 Track Fitting Formalism

I recommend reading [37], Chapter 4 of [38], and [39] in order to best understand the fitting algorithm. However, due to the at times confusing notation, ommitted equations or concepts, and differences between papers, I have attempted to summarize here the different sources and present the material in a more understandable and readable format. The implementation of the fitting algorithm into the code follows this section.

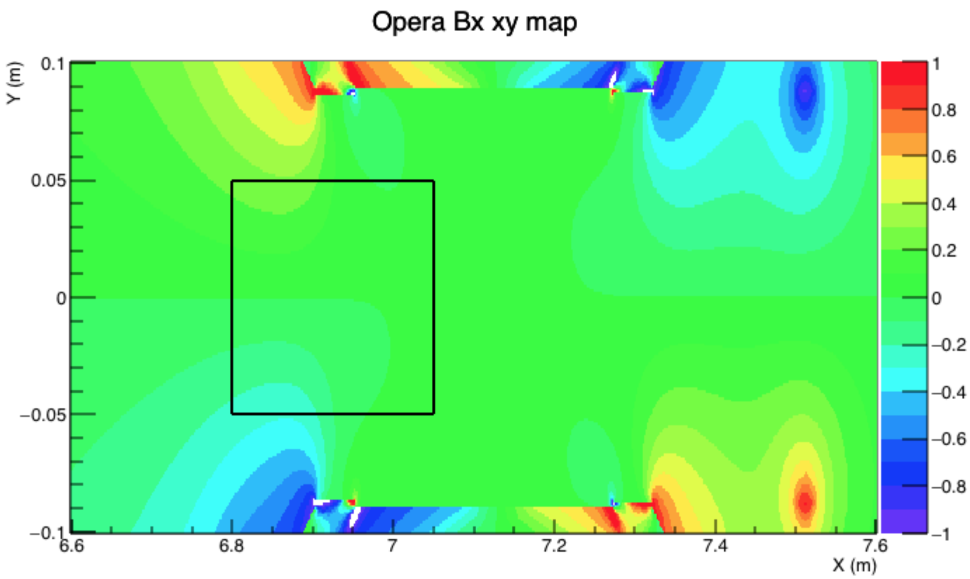

Figure 4·4: Shown is the radial field of the $g-2$ magnet in and around the storage region as calculated in Opera 2D. The center of the storage region lies at 7.112 m along the x axis. The black box shows the rough location of the tracker with respect to the field (size exaggerated slightly). It can be seen that there is a large homogeneity at the inner upper and lower ends compared to the right center. The shape of the pole pieces and tips can readily be seen.

One can define a χ^2 for a track in the usual way by dividing the residuals of measured and predicted track parameters by their errors:

$$\chi^2 = (\vec{p} - \vec{x})^T(\sigma^{-1})(\vec{p} - \vec{x}), \tag{4.1}$$

where $\vec{p}$ are predicted track parameters from a fit to the measured track parameters $\vec{x}$, and σ is a covariance matrix of errors on the fitted parameters. The Geant4 error propagation routines can be used to determine these predicted parameters and error matrices by propagating track parameters from some initial guesses. By minimizing this χ^2 with respect to the track parameters one can then fit and improve the track. The Geant4 error propagation routines propagate particles along their average trajectories neglecting the effects of discrete processes, using a helix equation along small enough steps where the change in the magnetic field is small. The predicted parameters are then a function of path length:

$$p_l = F_{l,l_0}(p_0), \tag{4.2}$$

where the path length can be defined how one wishes. In our system we have tracker planes defined at X positions, and limit path lengths to reach those planes. (From here on the dependence on path length or X position will be neglected, in favor of using plane indices.) In tandem, error matrices describing the expected distribution in true parameters about those predicted parameters due to said discrete process are also calculated:

$$\sigma^{ij} =< p^i p^j > - < p^i > \cdot < p^j >, \tag{4.3}$$

where i and j are track parameter indices. These parameter vectors are 5x1 objects defined in some track representation, as described in the Coordinate Systems section. The propagation of these parameters and error matrices are done using transport matrices, which express the infinitesimal changes in parameters at some plane (or path length) with respect to the parameters at some previous plane (or previous path length):

$$\delta p_N = T_{N,N-1} \delta p_{N-1}, \tag{4.4}$$

$$\sigma_N = T_{N,N-1} \sigma_{N-1} T^T_{N,N-1}. \tag{4.5}$$

Said transport and error matrices are 5x5 objects since the parameter vectors are 5x1 objects as described above. The calculation of these transport matrices, as well as details on the functional form of 4.2 are shown in [40].

With parameters defined on such planes, one can define the χ^2 as:

$$\chi^2 = \sum_{i=1}^{N} [(p_i(p) - x_i)^T (\sigma_i^{-1})(p_i(p) - x_i)], \tag{4.6}$$

where p_i are the average predicted parameters from some general starting parameters p. At first order one can solely include the measurement errors on parameters, which fill in the diagonals of σ_i, if random processes can be neglected. Unmeasured parameters should have measurement errors of infinity (or some large value) along the diagonals in the code, which account for the fact that residuals for unmeasured parameters do not exist. When the error matrix is inverted all rows and columns of the matrix with these large numbers will fall to 0 in the χ^2.

In order to get the best fit track, the χ^2 should be minimized with respect to the initial track parameters p, and evaluated at some chosen or fitted parameters:

$$\frac{\partial \chi^2}{\partial p}|_{p=p'_0} = 0, \tag{4.7}$$

resulting in

$$\begin{aligned}0 = \sum_{i=1}^{N}[(\frac{\partial p_i(p)}{\partial p}|_{p=p_0'})^T(\sigma_i^{-1})(p_i(p_0') - x_i) \\ +(p_i(p_0') - x_i)^T\frac{\partial(\sigma_i^{-1})}{\partial p}|_{p=p_0'}(p_i(p_0') - x_i) \\ +(p_i(p_0') - x_i)^T(\sigma_i^{-1})(\frac{\partial p_i(p)}{\partial p}|_{p=p_0'})]\end{aligned} \tag{4.8}$$

where the 1st and 3rd terms are identical, and the 2nd term is small if one assumes that the error matrix doesn't change much with respect to the starting parameters. (Fair since most of the error comes from measurement, and as long as the initial guess is decent enough such that the path length through material doesn't change appreciably from one iteration to the next.) This simplifies to:

$$\sum_{i=1}^{N} T_{i0}^T(\sigma_i^{-1})(p_i(p_0') - x_i) = 0, \tag{4.9}$$

which is just the top term with

$$T_{i0} = \frac{\partial p_i(p)}{\partial p}. \tag{4.10}$$

To solve this make the substitution

$$p_i(p_0') = p_i(p_0) + \frac{\partial p_i(p_0)}{\partial p}\Delta p_0 = p_i(p_0) + T_{i0}\Delta p_0, \tag{4.11}$$

where p_0' are the improved starting parameters for the next iteration calculated from the previous starting parameters p_0, and Δp_0 are the changes in the starting parameters to improve the track. This equation can be plugged into the above if one makes the assumption that T_{i0} does not change much from one iteration the next, which follows from the inherent nature of making small adjustments to the track in order to improve it.

After simplifying one arrives at

$$\Delta p_0 = \sigma_{p_0} \sum_{i=1}^{N} T_{i0}^{T}(\sigma_i^{-1})(x_i - p_i(p_0)), \tag{4.12}$$

where

$$\sigma_{p_0} = [\sum_{i=1}^{N} T_{i0}^{T}(\sigma_i^{-1})T_{i0}]^{-1}, \tag{4.13}$$

is the 5x5 covariance matrix of fitted parameters on the starting plane, whose diagonals describe the errors in the 5 track parameters on that plane and in the region close to it. (The fit does not directly return fit errors for track parameters on other planes.) Δp_0 along with χ^2 is exactly what we want to determine since that is what allows us to fit and improve the track from iteration to iteration.

However, since random processes should not be neglected for optimal tracking results, it makes more sense to return to the original χ^2 in equation 4.1, only now the included matrix and vector objects are combined into one large linear algebra equation. Instead of a sum over N 5x1 objects multiplying 5x5 error matrices, the vectors are combined into a single 5Nx1 vector multiplying a single 5Nx5N matrix. The 5x5 diagonal blocks of this large error matrix should now include the effects due to material processes as calculated in Geant from equation 4.3 as well as the measurement errors.

Because now parameters at one plane are no longer independent of the parameters at other planes, due to correlations from these random processes, it's necessary to add off-diagonal elements into the large error matrix. These 5x5 blocks come from

$$\sigma_{MN} = T_{MN}\sigma_N, \tag{4.14}$$

for the top diagonals, and the transpose for the bottom diagaonals, where M and N are two separate planes within the detector. (σ_N is the error matrix on plane N calculated from the starting plane.) This follows from equation 4.3 evaluated at plane M with respect to a path length from plane N, and not plane 0, which is equivalent to 4.14.

You can then minimize the χ^2 in the same way, only again with the matrix objects being aggregates of the per plane objects:

$$\Delta\vec{p}_0 = \sigma_{p_0}\tau^T\sigma^{-1}(\vec{x} - \vec{p}), \tag{4.15}$$

$$\sigma_{p_0} = [\tau^T\sigma^{-1}\tau]^{-1}, \tag{4.16}$$

where τ is the combined transport matrices from the individual 5x5 matrices, a 5Nx5 object.

The unmeasured parameter errors of infinity still come into play in the final calculation in the same was as before. Because however these matrix objects are very large, and the tracking must have a certain amount of speed in order to keep up with data, it is useful to reduce the size of these matrices. (It also makes things easier programming wise. Note that there are other some other ways to speed things up, specifically the banded inversion method as described in reference [39]. This method was not used in favor of getting the code working in the simpler form in the first place, but it is a possiblity in the future to use this technique to speed things up even more.) It suffices to simply remove all rows and columns where said infinity values exist in the error matrix. This is mathematically equivalent to inverting the error matrix with the infinities included, which make all rows and columns where they exist go to zero. The associated unmeasured parameter rows in the residual vector and transport matrices must similarly be removed. This results in an Nx1 residual vector, NxN error matrix, 5xN combined transport matrix transpose, which multiply against the 5x5 covariance matrix out front to still result in a 5x1 fix to the starting parameters, and a scalar χ^2 value. (Note that these element removals should be done just before the final calculation, and not higher up in the algrebra, otherwise plane correlations are not properly calculated.)

By calculating the last two equations one can fit the track, acquire a χ^2 describing the degree of the fit, determine how the track parameters can be improved at the starting point, and calculate errors on those starting parameters. This algorithm can be iterated a number of times to get a best fit track until successive iterations produce no improvement, where usually 3 or 4 iterations is enough. Note that there is remarkable robustness with respect to the initial starting parameters in fitting the track. Of course if the initial starting paramaters are too poor, then the fit will not converge. All of these calculations are completed within the GeaneFitter.cc file within the framework.

4.4 Track Extrapolation

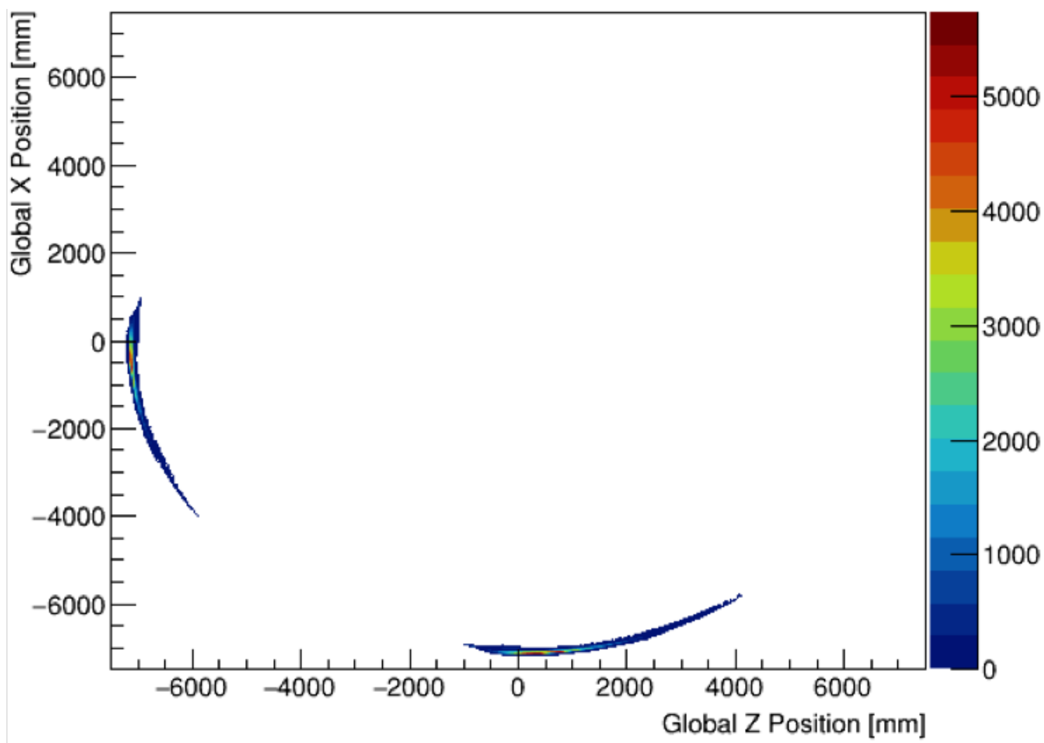

Figure 4·5: preliminary replace at some point

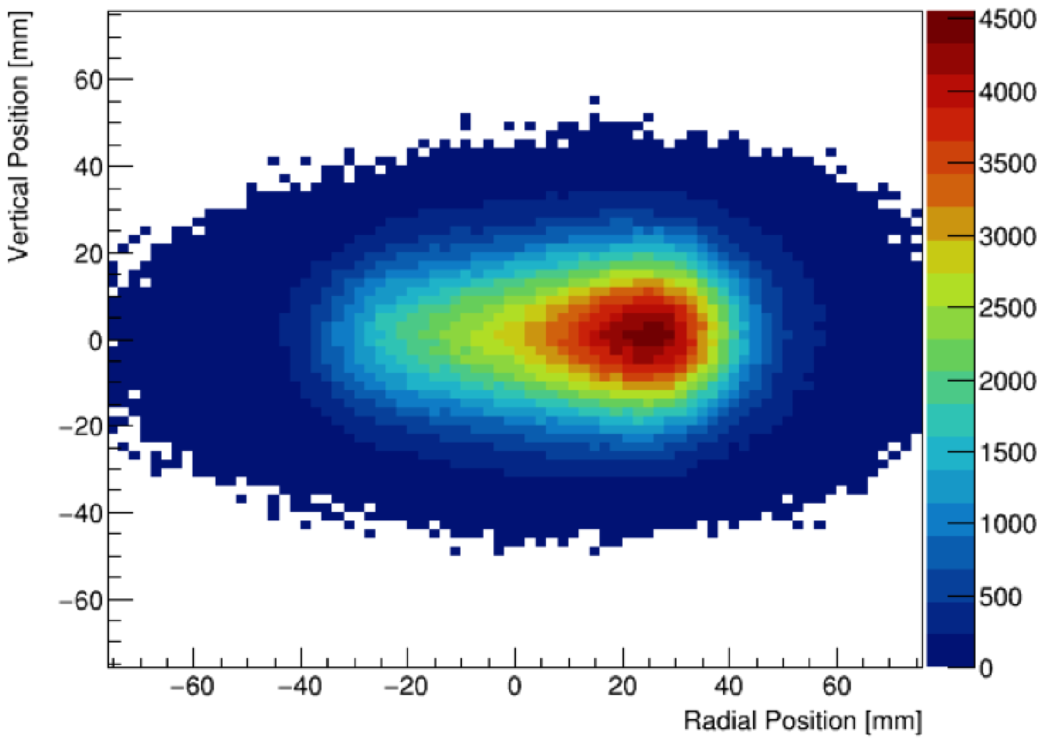

Figure 4·6: preliminary replace at some point

Chapter 5

ω_a Measurement

5.1 Data

5.2 Spectra Making

5.2.1 Clustering

5.2.2 Histogramming

5.3 Fitting

5.4 Systematic Errors

Chapter 6

Conclusion

6.1 Final Value

test4

Appendix A

g for Spin-1/2 Particles and Beyond

This was taken from my old HEP2 class report paper - go back and clean this up/improve it. If I end up not having time I can probably also just remove it.

The derivation contained here is taken and simplified from Reference [41]. Starting with the Dirac equation

$$(i\gamma^\mu \partial_\mu - m - e\gamma^\mu A_\mu)\psi = 0 \tag{A.1}$$

and multiplying by

$$(i\gamma^\mu \partial_\mu + m - e\gamma^\mu A_\mu)\psi = 0, \tag{A.2}$$

where the sign on m is reversed, you arrive at the equation

$$[(i\partial_\mu - eA_\mu)(i\partial_\nu - eA_\nu)\gamma^\mu\gamma^\nu - m^2]\psi = 0. \tag{A.3}$$

This can be split this into its symmetric and antisymmetric parts:

$$\begin{aligned}&(\frac{1}{4}\{i\partial_\mu - eA_\mu, i\partial_\nu - eA_\nu\}\{\gamma^\mu, \gamma^\nu\}\\ &+\frac{1}{4}[i\partial_\mu - eA_\mu, i\partial_\nu - eA_\nu][\gamma^\mu, \gamma^\nu] - m^2)\psi = 0\end{aligned} \tag{A.4}$$

Using the identities

$$\frac{i}{2}[\gamma^\mu, \gamma^\nu] = \sigma^{\mu\nu} \tag{A.5}$$

and

$$[i\partial_\mu - eA_\mu, i\partial_\nu - eA_\nu]$$
$$= -ie[\partial_\mu A_\nu - \partial_\nu A_\nu] = -ieF_{\mu\nu} \tag{A.6}$$

where $\sigma^{\mu\nu}$ is related to the spin of the particle and $F_{\mu\nu}$ is the electromagnetic field tensor, one arrives at the form

$$((i\partial_\mu - eA_\mu)^2 - \frac{e}{2}F_{\mu\nu}\sigma^{\mu\nu} - m^2)\psi = 0. \tag{A.7}$$

Expanding out the tensor objects

$$\frac{e}{2}F_{\mu\nu}\sigma^{\mu\nu} = -e\begin{pmatrix}(\vec{B}+i\vec{E})\cdot\vec{\sigma} & \\ & (\vec{B}-i\vec{E})\cdot\vec{\sigma}\end{pmatrix} \tag{A.8}$$

and forming a new covariant derivative

$$\not{D}^2 = D_\mu^2 + \frac{e}{2}F_{\mu\nu}\sigma^{\mu\nu} \tag{A.9}$$

where D_μ^2 is your ordinary covariant derivative, by moving to momentum space you can arrive at the equation

$$\frac{(H+eA)^2}{2m}\psi = (\frac{m}{2} + \frac{(\vec{p}+e\vec{A})^2}{2m} - 2\frac{e}{2m}\vec{B}\cdot\vec{s} \pm i\frac{e}{m}\vec{E}\cdot\vec{s})\psi. \tag{A.10}$$

Lo and behold, you have arrived at the Dirac g = 2 result, contained in front of the magnetic piece in the form of Equation **??**.

How then does such a term change at loop level? Most generally the vertex of a particle interacting with a magnetic field through the mediation of a photon can be represented by

$$iM^\mu = \bar{u}(q_2)(f_1\gamma^\mu + f_2 p^\mu + f_3 q_1^\mu + f_4 q_2^\mu)u(q_1) \tag{A.11}$$

where q_1 and q_2 are the ingoing and outgoing four-momenta respectively, which can be constrained on-shell, and p is the four-momenta of the photon, which is off-shell. The f_i are in general contractions of four-momenta and gamma matrices. By using the Gordon identity

$$\begin{aligned} &\bar{u}(q_2)(q_1^\mu + q_2^\mu)u(q_1) \\ = (2m)\bar{u}(q_2)\gamma^\mu u(q_1) + i\bar{u}(q_2)\sigma^{\mu\nu}&(q_1^\nu - q_2^\nu)u(q_1) \end{aligned} \tag{A.12}$$

any Feynman diagram can be reorganized into the form

$$iM^\mu = (-ie)\bar{u}[F_1(\frac{p^2}{m^2})\gamma^\mu + \frac{i\sigma^{\mu\nu}}{2m}p_\nu F_2(\frac{p^2}{m^2})]u, \tag{A.13}$$

where F_1 and F_2 are form factors. One notices that the F_2 piece is reminiscent of our magnetic dipole moment form that we derived from the Dirac equation. So the problem now becomes for any Feynman diagram calculation in any theory, at any order, to solve for this F_2 to determine the contribution to the magnetic dipole moment.

Appendix B

Ratio Method Derivation

B.1 Ratio Form and Function

Consider the 5 parameter function:

$$N_5(t) = N_0 e^{-t/\tau}(1 + A\cos(\omega_a t + \phi)), \tag{B.1}$$

which describes some ideal dataset in histogram format. Here ϕ will be set to zero for simplicity. Now define the variables $u_+(t)$, $u_-(t)$, $v_1(t)$, and $v_2(t)$ as

$$\begin{aligned} u_+(t) &= \frac{1}{4}N_5(t + T/2) \\ u_-(t) &= \frac{1}{4}N_5(t - T/2) \\ v_1(t) &= \frac{1}{4}N_5(t) \\ v_2(t) &= \frac{1}{4}N_5(t), \end{aligned} \tag{B.2}$$

where the 1/4 out front reflects randomly splitting the whole dataset into 4 equally weighted sub-datasets, and T is the g-2 period known to high precision, $\mathcal{O}(10^{-6})$. This corresponds to a weighting of 1:1:1:1 between the datasets. To be explicit here regarding the signs, the counts that are filled into the histogram described by u_+ have their times shifted as $t \to t - T/2$, which is what the function $N_5(t + T/2)$ describes, and vice versa for u_-. To form the ratio define the variables:

$$\begin{aligned} U(t) &= u_+(t) + u_-(t) \\ V(t) &= v_1(t) + v_2(t) \\ R(t) &= \frac{V(t) - U(t)}{V(t) + U(t)}. \end{aligned} \tag{B.3}$$

Plugging in and dividing the common terms $(N_0 e^{-t/\tau}/4)$,

$$R(t) = \frac{2(1 + A\cos(\omega_a t)) - e^{-T/2\tau}(1 + A\cos(\omega_a t + \omega_a T/2)) - e^{T/2\tau}(1 + A\cos(\omega_a t - \omega_a T/2))}{2(1 + A\cos(\omega_a t)) + e^{-T/2\tau}(1 + A\cos(\omega_a t + \omega_a T/2)) + e^{T/2\tau}(1 + A\cos(\omega_a t + \omega_a T/2))}. \tag{B.4}$$

Now set $\omega_a T/2 = \delta$, and note that T is really

$$\begin{aligned} T = T_{guess} &= \frac{2\pi}{\omega_a} + \Delta T, \\ \Delta T &= T_{guess} - T_{true}. \end{aligned} \tag{B.5}$$

Being explicit,

$$\delta = \frac{\omega_a}{2} T_{guess} = \frac{\omega_a}{2}(\frac{2\pi}{\omega_a} + \Delta T) = \pi + \pi\frac{\Delta T}{T_{true}} = \pi + \pi(\delta T), \tag{B.6}$$

and δ can be redefined as

$$\delta = \pi(\delta T), \tag{B.7}$$

by flipping the sign of any cosine terms that contain δ.

Then, using the trig identity

$$\cos(a \pm b) = \cos(a)\cos(b) \mp \sin(a)\sin(b) \tag{B.8}$$

so that

$$\begin{aligned}\cos(\omega_a t \pm \delta) &= \cos(\omega_a t)\cos\delta \mp \sin(\omega_a t)\sin\delta \\ &\approx \cos(\omega_a t)(1-\delta^2) \mp \sin(\omega_a t)\delta \\ &\approx \cos(\omega_a t),\end{aligned} \tag{B.9}$$

since $\delta \sim O(10^{-5})$, the ratio becomes

$$R(t) \approx \frac{2(1 + A\cos(\omega_a t)) - (1 - A\cos(\omega_a t))(e^{-T/2\tau} + e^{T/2\tau})}{2(1 + A\cos(\omega_a t)) + (1 - A\cos(\omega_a t))(e^{-T/2\tau} + e^{T/2\tau})}. \tag{B.10}$$

Expanding

$$e^{\pm T/2\tau} = 1 \pm \frac{T}{2\tau} + \frac{1}{2}\left(\frac{T}{2\tau}\right)^2 \pm \ldots, \tag{B.11}$$

repacing and simplifying,

$$R(t) \approx \frac{A\cos(\omega_a t) - C(1 - A\cos(\omega_a t))}{1 + C(1 - A\cos(\omega_a t))}, \tag{B.12}$$

where

$$C = \frac{1}{16}\left(\frac{T}{\tau}\right)^2 \approx 2.87 * 10^{-4}. \tag{B.13}$$

Using the expansion

$$f(x) = \frac{1}{1+x} = 1 - x + x^2 - \ldots, \quad |x| < 1, \tag{B.14}$$

and since C is small, the denominator can be manipulated such that

$$\begin{aligned}R(t) &\approx (A\cos(\omega_a t)) - C(1 - A\cos(\omega_a t)))(1 - C(1 - A\cos(\omega_a t))) \\ &\approx A\cos(\omega_a t) - C + CA^2\cos^2(\omega_a t),\end{aligned} \tag{B.15}$$

after dropping terms of $\mathcal{O}(C^2)$ and higher. In practice the last term is ommitted since it has a minimal effect on the fitted value of ω_a [**cite**], and one arrives at

$$R(t) \approx A\cos(\omega_a t) - C, \tag{B.16}$$

the conventional 3 parameter ratio function.

In order to avoid approximations one can instead weight the counts in the histograms as

$$u_+(t) : u_-(t) : v_1(t) : v_2(t) = e^{T/2\tau} : e^{-T/2\tau} : 1 : 1, \tag{B.17}$$

so that

$$\begin{aligned}
u_+(t) &= \frac{e^{T/2\tau}}{2 + e^{T/2\tau} + e^{-T/2\tau}} N_5(t + T/2) \\
u_-(t) &= \frac{e^{-T/2\tau}}{2 + e^{T/2\tau} + e^{-T/2\tau}} N_5(t - T/2) \\
v_1(t) &= \frac{1}{2 + e^{T/2\tau} + e^{-T/2\tau}} N_5(t) \\
v_2(t) &= \frac{1}{2 + e^{T/2\tau} + e^{-T/2\tau}} N_5(t).
\end{aligned} \tag{B.18}$$

(These factors out front aren't so far off from 1/4 since $e^{\pm T/2\tau} \approx e^{\pm 4.35/2*64.4} \approx 1.034, .967$.) Then instead $R(t)$ becomes

$$R(t) = \frac{2(1 + A\cos(\omega_a t)) - (1 - A\cos(\omega_a t + \delta)) - (1 - A\cos(\omega_a t - \delta))}{2(1 + A\cos(\omega_a t)) + (1 - A\cos(\omega_a t + \delta)) + (1 - A\cos(\omega_a t + \delta))}, \tag{B.19}$$

where the $e^{\pm T/2\tau}$ terms out front now cancel. Using Equation B.9 again and this time avoiding approximations in δ,

$$R(t) = \frac{2A\cos(\omega_a t)(1 + \cos\delta)}{4 + 2A\cos(\omega_a t)(1 - \cos\delta)}, \tag{B.20}$$

after simplifying. In the limit that

$$\delta = \pi(\delta T) \to 0 \tag{B.21}$$

since δT is small,

$$R(t) \approx A\cos(\omega_a t), \tag{B.22}$$

with the only approximation being made at $\mathcal{O}(\delta^2) \sim \mathcal{O}(10^{-10})$.

Finally, while the 3 parameter ratio function suffices for fits to data containing slow modulations, it does not suffice for faster oscillation features. In that case it is more useful to fit with the non-approximated or simplified version of the ratio,

$$\begin{aligned} R(t) &= \frac{v_1(t) + v_2(t) - u_+(t) - u_-(t)}{v_1(t) + v_2(t) + u_+(t) + u_-(t)}, \\ &= \frac{2f(t) - f_+(t) - f_-(t)}{2f(t) + f_+(t) + f_-(t)}, \end{aligned} \tag{B.23}$$

where

$$\begin{aligned} f(t) &= C(t)(1 + A\cos(\omega_a t + \phi)) \\ f_\pm(t) &= f(t \pm T_a/2), \end{aligned} \tag{B.24}$$

and $C(t)$ can encode any other effects in the data that need to be fitted for, such as the CBO,

$$C(t) = 1 + A_{cbo} \cdot e^{-t/\tau_{cbo}} \cdot \cos(\omega_{cbo} t + \phi_{cbo}). \tag{B.25}$$

Additionally, any other fit parameters such as A or ϕ can be made a fuction of t. Using the non-approximated form for the final fit function gives greater confidence in the fit results for the high precision ω_a extraction necessary for the experimental measurement.

B.2 Ratio Point Errors

In order to determine the errors on the points in the formed ratio, Equation B.3, we use standard error propagation:

$$\sigma_R(t)^2 = \Big(\frac{\partial R(t)}{\partial V(t)}\Big)^2 \delta V(t)^2 + \Big(\frac{\partial R(t)}{\partial U(t)}\Big)^2 \delta U(t)^2 \tag{B.26}$$

This works because $V(t)$ and $U(t)$ are statistically independent datasets. Using standard error propagation again,

$$\begin{aligned} \delta V(t)^2 &= \delta v_1(t)^2 + \delta v_2(t)^2 = v_1(t) + v_2(t) = V(t), \\ \delta U(t)^2 &= \delta u_+(t)^2 + \delta u_-(t)^2 = u_+(t) + u_-(t) = U(t). \end{aligned} \tag{B.27}$$

Calculating out and simplifying the partial derivatives, (and this time dropping the t's),

$$\begin{aligned} \frac{\partial R}{\partial V} &= \frac{2U}{(V+U)^2}, \\ \frac{\partial R}{\partial U} &= \frac{-2V}{(V+U)^2}. \end{aligned} \tag{B.28}$$

Combining and simplifying, we arrive at the error formula:

$$\sigma_R^2 = \frac{4UV}{(V+U)^3} = \frac{1-R^2}{(V+U)} \tag{B.29}$$

Appendix C

Pileup Modified Errors

In the pileup subtraction method detailed in Section **??**, pileup events are statistically constructed and then subtracted from the data. Because of this, the errors on the bins need to be adjusted appropriately. Reference [42] describes the modified errors, but is not quite correct. Here is provided an improved calculation that I believe is easier to understand. While we are mainly interested in the errors on the histogram bins after pileup subtraction, it first helps to examine the errors of the pileup histogram itself. Here we only consider doublets.

In the aysmmetric shadow window pileup method, shadow doublets are constructed from two singlets. The pileup histogram is then filled as the sum of the doublets minus the singlets,

$$P = D - S, \tag{C.1}$$

where D or S are only added or subtracted when they are above some energy threshold. If the threshold is set to 0, then for every doublet one entry will be added and two will be subtracted. Since these entries are exactly correlated, the error in each time bin will be

$$\sigma_P = \sqrt{N_D}, \tag{C.2}$$

where N_D is the number of doublets in that time bin. If the energy threshold is above 0, then we can determine whether the counts in the pileup histogram increase

	$E_1 < E_{th}$	$E_1 > E_{th}$
$E_2 < E_{th}$	$N_1(+1)$	$N_2(0)$
$E_2 > E_{th}$	$N_3(0)$	$N_4(-1)$

Table C.1: Table of doublets above threshold. Here E_1 and E_2 are the energies of the two singlets, E_{th} is the energy threshold, and N_i are the number of doublets above threshold for the different combinations of E_1 and E_2. (N_1 is assumed above threshold here.) The numbers in the parentheses indicate the number of counts gained or lost in the pileup histogram.

or decrease based on whether the singlets and doublets are above threshold or not. Table C.1 shows the different combinations of counts put into the pileup histogram. The counts that go into P will be

$$\begin{aligned} P &= \sum_i N_i - \text{singlets above threshold} \\ &= (N_1 + N_2 + N_3 + N_4) - (N_2 + N_4) - (N_3 + N_4) \\ &= N_1 - N_4 \end{aligned} \tag{C.3}$$

and the errors are

$$\sigma_P = \sqrt{N_1 + N_4}. \tag{C.4}$$

This makes sense considering the cases individually. In the cases for N_1, you will gain a count from the doublet above threshold, and lose no counts since both singlets are below threshold. In the cases for N_2 and N_3, you will gain a count from the doublet, and lose a count from one of the singlets which is above threshold. In the cases for N_4, you will gain a count from the doublet and lose two counts from the singlets which are both above threshold. Since the doublet and singlets are exactly correlated, the N_1 and N_4 cases naturally result in a single weight being added into the error, while the N_2 and N_3 cases result in no additions to the error.

Now what about the pileup subtracted time spectrum? Our corrected spectrum can be written as

$$N_{\text{corrected}} = N_{\text{measured}} - P. \tag{C.5}$$

What is in N_{measured} doesn't matter exactly. What we care about is what is in N_{measured} that is also within P, for that is where the correlations come from. Since N_{measured} is the sum of all singlets above threshold, we can write it as

$$N_{\text{measured}} = N_{\text{other}} + N_2 + N_3 + 2N_4 \tag{C.6}$$

since we know that those cases N_i listed come from singlets above threshold, and N_{other} is anything in the measured hits that was not included in the pileup shadow construction. We can then replace P and simplify to get

$$N_{\text{corrected}} = N_{\text{other}} - N_1 + N_2 + N_3 + 3N_4. \tag{C.7}$$

The error on the corrected histogram is then

$$\sigma_{N_{\text{corrected}}} = \sqrt{N_{\text{other}} + N_1 + N_2 + N_3 + 9N_4}. \tag{C.8}$$

Replacing N_{other} as

$$N_{\text{other}} = N_{\text{corrected}} + N_1 - N_2 - N_3 - 3N_4, \tag{C.9}$$

we can remove the dependence of the corrected histogram errors on the unknown quantity and arrive at

$$\begin{aligned} \sigma_{N_{\text{corrected}}} &= \sqrt{N_{\text{corrected}} + 2N_1 + 6N_4}, \\ &= \sqrt{N_{\text{corrected}}} \cdot \sqrt{1 + (2N_1 + 6N_4)/N_{\text{corrected}}}. \end{aligned} \tag{C.10}$$

(This argument might seem circular at the end, but it works because of the squaring that occurs when calculating the error.) In the end we have a form for the bin errors of the pileup corrected histogram which only depend on N_1 and N_4 in addition to the number of counts in the corrected histogram. As shown it can be refactored into a form equal to the naive errors (just the bin content) times some correction factor. Since N_1 and N_4 are much smaller than $N_{\text{corrected}}$ at all times, and because they decay away at about twice the rate as the pileup diminishes, the change to the errors is small, of the order 1 or 2% at 30 µs.

C.1 For the ratio function

Equation C.10 applies to the corrected errors for a pileup subtracted histogram, but what about the modifications to the ratio errors? If we parameterize that equation as

$$\sigma_{N_{\text{corrected}}} = \sqrt{N_{\text{corrected}}} \cdot \sqrt{\gamma(t)}, \tag{C.11}$$

where the correction factor $\gamma(t) \approx \gamma e^{-t/\tau_\mu}$ is small and decays at approximately the muon lifetime, we can recast the errors on the individual ratio sub-datasets as

$$\begin{aligned}
\delta V(t)^2 &= \delta v_1(t)^2 \cdot \gamma(t) + \delta v_2(t)^2 \cdot \gamma(t) = (v_1(t) + v_2(t)) \cdot \gamma(t) = V(t) \cdot \gamma(t), \\
\delta U(t)^2 &= \delta u_+(t)^2 \cdot \gamma(t + T/2) + \delta u_-(t)^2 \cdot \gamma(t - T/2) \\
&\approx u_+(t) \cdot \gamma(t) e^{-T/2\tau} + u_-(t) \cdot \gamma(t) e^{+T/2\tau} \\
&\approx (u_+(t) + u_-(t)) \cdot \gamma(t) \cdot \left(1 + \frac{1}{2}\left(\frac{T}{2\tau}\right)^2\right) \\
&\approx U(t) \cdot \gamma(t),
\end{aligned} \tag{C.12}$$

where in the last step the $\frac{1}{2}\left(\frac{T}{2\tau}\right)^2$ term has been neglected because it's small. With these approximations having been made, the modified errors on the ratio points simply become

$$\sigma_R^2 \to \sigma_R^2 \cdot \gamma(t), \tag{C.13}$$

with the correction being the same as that on the pileup subtracted histogram. Credit to Reference [43] for this derivation.

Bibliography

[1] P. Dirac. "The quantum theory of the electron". In: *Proceedings of the Royal Society of London* Series A, Containing Papers of a Mathematical and Physical Character (1928).

[2] J. E. Nafe, E. B. Nelson, and I. I. Rabi. "The Hyperfine Structure of Atomic Hydrogen and Deuterium". In: *Phys. Rev.* 71 (12 June 1947), pp. 914–915. DOI: 10.1103/PhysRev.71.914. URL: https://link.aps.org/doi/10.1103/PhysRev.71.914.

[3] Julian Schwinger. "On Quantum-Electrodynamics and the Magnetic Moment of the Electron". In: *Phys. Rev.* 73 (4 Feb. 1948), pp. 416–417. DOI: 10.1103/PhysRev.73.416. URL: https://link.aps.org/doi/10.1103/PhysRev.73.416.

[4] Tatsumi Aoyama et al. "Complete Tenth-Order QED Contribution to the Muon g-2". In: *Phys. Rev. Lett.* 109 (2012), p. 111808. DOI: 10.1103/PhysRevLett.109.111808. arXiv: 1205.5370 [hep-ph].

[5] Tatsumi Aoyama, Toichiro Kinoshita, and Makiko Nio. "Revised and Improved Value of the QED Tenth-Order Electron Anomalous Magnetic Moment". In: *Phys. Rev.* D97.3 (2018), p. 036001. DOI: 10.1103/PhysRevD.97.036001. arXiv: 1712.06060 [hep-ph].

[6] Joshua Ellis. "TikZ-Feynman: Feynman diagrams with TikZ". In: *Comput. Phys. Commun.* 210 (2017), pp. 103–123. DOI: 10.1016/j.cpc.2016.08.019. arXiv: 1601.05437 [hep-ph].

[7] Max Dohse. "TikZ-FeynHand: Basic User Guide". In: (2018). arXiv: 1802.00689 [cs.OH].

[8] C. Gnendiger, D. Stöckinger, and H. Stöckinger-Kim. "The electroweak contributions to $(g-2)_\mu$ after the Higgs boson mass measurement". In: *Phys. Rev.* D88 (2013), p. 053005. DOI: 10.1103/PhysRevD.88.053005. arXiv: 1306.5546 [hep-ph].

[9] Tadashi Ishikawa, Nobuya Nakazawa, and Yoshiaki Yasui. "Numerical calculation of the full two-loop electroweak corrections to muon (g-2)". In: (2018). arXiv: 1810.13445 [hep-ph].

[10] F. Jegerlehner. *The Anomalous Magnetic Moment of the Muon.* Springer Tracts in Modern Physics. Springer Berlin Heidelberg, 2007. ISBN: 9783540726340. URL: https://books.google.com/books?id=uxQj004Py6AC.

[11] D. Babusci et al. "Precision measurement of $\sigma(e^+e^- \to \pi^+\pi^-\gamma)/\sigma(e^+e^- \to \mu^+\mu^-\gamma)$ and determination of the $\pi^+\pi^-$ contribution to the muon anomaly with the KLOE detector". In: *Phys. Lett.* B720 (2013), pp. 336–343. DOI: 10.1016/j.physletb.2013.02.029. arXiv: 1212.4524 [hep-ex].

[12] T. Xiao et al. "Precision Measurement of the Hadronic Contribution to the Muon Anomalous Magnetic Moment". In: *Phys. Rev.* D97.3 (2018), p. 032012. DOI: 10.1103/PhysRevD.97.032012. arXiv: 1712.04530 [hep-ex].

[13] Bogdan Malaescu. "Measurement of hadronic cross sections at BABAR with ISR and implications for the muon (g-2)". In: *Proceedings, International Conference on the Structure and the Interactions of the Photon including the 20th International Workshop on Photon-Photon Collisions and the International Workshop on High Energy Photon Linear Colliders, PHOTON 2013: Paris, France, May 20-24, 2013.* 2014. arXiv: 1404.6887 [hep-ex]. URL: http://www-public.slac.stanford.edu/sciDoc/docMeta.aspx?slacPubNumber=SLAC-PUB-16106.

[14] M. Ablikim et al. "Measurement of the $e^+e^- \to \pi^+\pi^-$ cross section between 600 and 900 MeV using initial state radiation". In: *Phys. Lett.* B753 (2016), pp. 629–638. DOI: 10.1016/j.physletb.2015.11.043. arXiv: 1507.08188 [hep-ex].

[15] Alexander Keshavarzi, Daisuke Nomura, and Thomas Teubner. "Muon $g-2$ and $\alpha(M_Z^2)$: a new data-based analysis". In: *Phys. Rev.* D97.11 (2018), p. 114025. DOI: 10.1103/PhysRevD.97.114025. arXiv: 1802.02995 [hep-ph].

[16] Michel Davier et al. "Reevaluation of the hadronic vacuum polarisation contributions to the Standard Model predictions of the muon $g-2$ and $\alpha(m_Z^2)$ using newest hadronic cross-section data". In: *Eur. Phys. J.* C77.12 (2017), p. 827. DOI: 10.1140/epjc/s10052-017-5161-6. arXiv: 1706.09436 [hep-ph].

[17] T. Blum et al. "Calculation of the Hadronic Vacuum Polarization Contribution to the Muon Anomalous Magnetic Moment". In: *Phys. Rev. Lett.* 121 (2 July 2018), p. 022003. DOI: 10.1103/PhysRevLett.121.022003. URL: https://link.aps.org/doi/10.1103/PhysRevLett.121.022003.

[18] Nils Asmussen et al. "Hadronic light-by-light scattering in the anomalous magnetic moment of the muon". In: *15th International Workshop on Tau Lepton Physics (TAU2018) Amsterdam, Netherlands, September 24-28, 2018.* 2018. arXiv: 1811.08320 [hep-lat].

[19] Andreas Nyffeler. "Precision of a data-driven estimate of hadronic light-by-light scattering in the muon $g-2$: Pseudoscalar-pole contribution". In: *Phys. Rev.* D94.5 (2016), p. 053006. DOI: 10.1103/PhysRevD.94.053006. arXiv: 1602.03398 [hep-ph].

[20] B. Lee Roberts. "The History of the Muon $(g-2)$ Experiments". In: *15th International Workshop on Tau Lepton Physics (TAU2018) Amsterdam, Netherlands, September 24-28, 2018*. 2018. arXiv: 1811.06974 [hep-ex].

[21] G. W. Bennett et al. "Final Report of the Muon E821 Anomalous Magnetic Moment Measurement at BNL". In: *Phys. Rev.* D73 (2006), p. 072003. DOI: 10.1103/PhysRevD.73.072003. arXiv: hep-ex/0602035 [hep-ex].

[22] D. Hanneke, S. Fogwell, and G. Gabrielse. "New Measurement of the Electron Magnetic Moment and the Fine Structure Constant". In: *Phys. Rev. Lett.* 100 (2008), p. 120801. DOI: 10.1103/PhysRevLett.100.120801. arXiv: 0801.1134 [physics.atom-ph].

[23] Peter J. Mohr, David B. Newell, and Barry N. Taylor. "CODATA recommended values of the fundamental physical constants: 2014". In: *Rev. Mod. Phys.* 88 (3 Sept. 2016), p. 035009. DOI: 10.1103/RevModPhys.88.035009. URL: https://link.aps.org/doi/10.1103/RevModPhys.88.035009.

[24] J. Jackson. *Classical Electrodynamics*. Wiley Indiana, 2011.

[25] W. Liu et al. "High Precision Measurements of the Ground State Hyperfine Structure Interval of Muonium and of the Muon Magnetic Moment". In: *Phys. Rev. Lett.* 82 (4 Jan. 1999), pp. 711–714. DOI: 10.1103/PhysRevLett.82.711. URL: https://link.aps.org/doi/10.1103/PhysRevLett.82.711.

[26] E. D. Commins and P. H. Bucksbaum. *Weak interactions of leptons and quarks*. Cambridge University Press, 1983.

[27] J. Grange et al. "Muon (g-2) Technical Design Report". In: (2015). arXiv: 1501.06858 [physics.ins-det].

[28] Diktys Stratakis et al. "Accelerator performance analysis of the Fermilab Muon Campus". In: *Phys. Rev. Accel. Beams* 20.11 (2017), p. 111003. DOI: 10.1103/PhysRevAccelBeams.20.111003. arXiv: 1803.00597 [physics.acc-ph].

[29] Cary Yoshikawa et al. "Optimization of the Target Subsystem for the New g-2 Experiment". In: (Jan. 2013).

[30] A. Yamamoto et al. "The superconducting inflector for the BNL g-2 experiment". In: *Nucl. Instrum. Meth.* A491 (2002), pp. 23–40. DOI: 10.1016/S0168-9002(02)01232-9.

[31] A. T. Fienberg et al. "Studies of an array of PbF_2 Cherenkov crystals with large-area SiPM readout". In: *Nucl. Instrum. Meth.* A783 (2015), pp. 12–21. DOI: 10.1016/j.nima.2015.02.028. arXiv: 1412.5525 [physics.ins-det].

[32] J. Kaspar et al. "Design and performance of SiPM-based readout of PbF_2 crystals for high-rate, precision timing applications". In: *JINST* 12.01 (2017), P01009. DOI: 10.1088/1748-0221/12/01/P01009. arXiv: 1611.03180 [physics.ins-det].

[33] David A. Sweigart. “A new MicroTCA-based waveform digitizer for the Muon g-2 experiment”. In: *PoS* ICHEP2016 (2016), p. 845. DOI: 10.22323/1.282.0845. arXiv: 1612.05145 [physics.ins-det].

[34] A. Anastasi et al. “Test of candidate light distributors for the muon $(g-2)$ laser calibration system”. In: *Nucl. Instrum. Meth.* A788 (2015), pp. 43–48. DOI: 10.1016/j.nima.2015.03.071. arXiv: 1504.00132 [physics.ins-det].

[35] A. Anastasi et al. “Electron beam test of key elements of the laser-based calibration system for the muon $g-2$ experiment”. In: *Nucl. Instrum. Meth.* A842 (2017), pp. 86–91. DOI: 10.1016/j.nima.2016.10.047. arXiv: 1610.03210 [physics.ins-det].

[36] A. Anastasi et al. “The laser control of the muon $g-2$ experiment at Fermilab”. In: *JINST* 13.02 (2018), T02009. DOI: 10.1088/1748-0221/13/02/T02009.

[37] V. Innocente, M. Maire, and E. Nagy. “GEANE: Average tracking and error propagation package”. In: *MC 91: Detector and event simulation in high-energy physics. Proceedings, Workshop, Amsterdam, Netherlands, April 8-12, 1991.* 1991, pp. 58–78. URL: http://innocentonnice.web.cern.ch/innocentonnice/napoli99/geane_manual.ps.

[38] Lia Lavezzi. “The fit of nuclear tracks in high precision spectroscopy experiments”. pp. 57-86. PhD thesis. Pavia U., 2007. URL: http://bamboo.pv.infn.it/doc/L_Lavezzi.pdf.

[39] V. Innocente and E. Nagy. “Trajectory fit in presence of dense materials”. In: *Nucl. Instrum. Meth.* A324 (1993), pp. 297–306. DOI: 10.1016/0168-9002(93)90992-Q.

[40] A. Strandlie and W. Wittek. “Derivation of Jacobians for the propagation of covariance matrices of track parameters in homogeneous magnetic fields”. In: *Nucl. Instrum. Meth.* A566 (2006), pp. 687–698.

[41] M. Schwartz. *Quantum Field Theory and the Standard Model*. Cambridge University Press, 2014.

[42] F. Farley et al. *Estimation of Error in Differential Pileup Subtracted Data*. E821 Muon g-2 Note 377. 2018.

[43] J. Paley. “Measurement of the Anomalous Magnetic Moment of the Negative Muon to 0.7 Parts Per Million”. PhD thesis. Boston University, 2004.

CURRICULUM VITAE

Joe Graduate

Basically, this needs to be worked out by each individual, however the same format, margins, typeface, and type size must be used as in the rest of the dissertation.